Supplementary Information

Endocranial anatomy of the giant extinct Australian mihirung birds (Aves, Dromornithidae)

Warren D. Handley[1]* and Trevor H. Worthy[1]

[1]Palaeontology Group, Flinders University, GPO 2100, Adelaide, SA, 5001, Australia. Email: warren.handley@flinders.edu.au; trevor.worthy@flinders.edu.au

* Correspondence: warren.handley@flinders.edu.au

S1 Credits for use of the Australian and New Zealand continental outlines, and silhouettes from Phylopic.org and New Zealand Birds Online in Figure S15

Australian map outline, freely available from: https://www.timvandevall.com/wp-content/uploads/australia-map-blank.jpg

New Zealand map outline by John Moen, freely available from: https://www.worldatlas.com/webimage/countrys/oceania/outline/nzout.htm

Dinornis robustus (as *Dinornis*) by anonymous, licence Public Domain Dedication 1.0

Dromornithid (as *Dromornis*) by Zimices, licence Creative Commons Attribution-NonCommercial 3.0 Unported

Stout-legged moa (*Euryapteryx curtus gravis*) adapted from Szabo [178] 'Stout-legged moa'. New Zealand Birds Online. http://www.nzbirdsonline.org.nz/species/stout-legged-moa

Note: a representative silhouette for *E. c. gravis* was not available from Phylopic.org, which only provides a silhouette for the Superfamily Emeidae by T. Michael Keesey (see http://phylopic.org/image/17c736b8-ca70-4edf-a7ca-71995e43e93f/) available under the licence https://creativecommons.org/publicdomain/zero/1.0/. However, this silhouette is not particularly descriptive of the known graviportal morphology of *E. c gravis*. Therefore, a more representative silhouette for the species was adapted from an image of a model provided by Szabo [177] freely available from the New Zealand Birds Online website (see link above), maintained by the Museum of New Zealand Te Papa Tongarewa, Wellington, New Zealand.

Dromaius novaehollandiae by Darren Naish (vectorized by T. Michael Keesey), licence https://creativecommons.org/licenses/by/3.0/

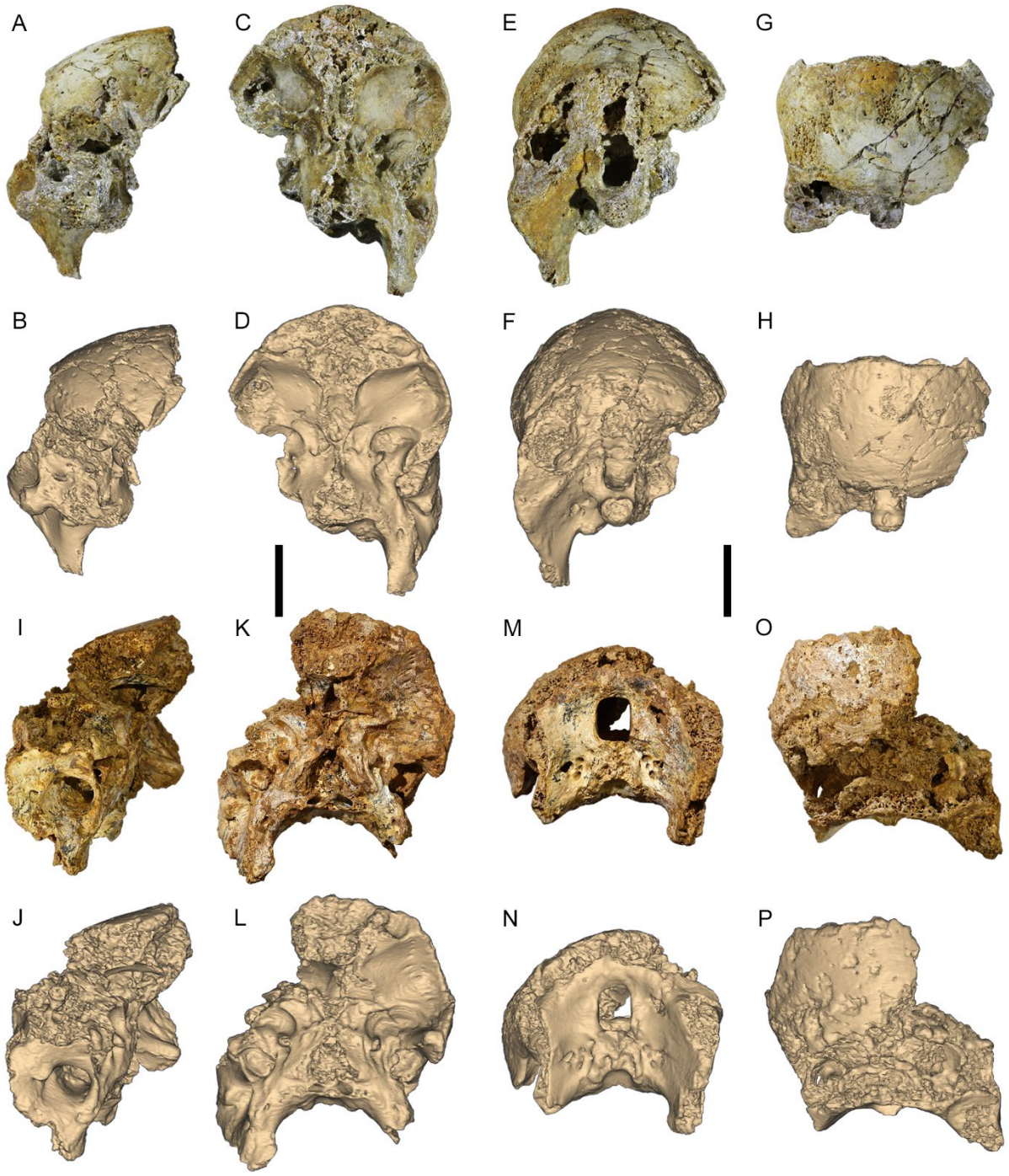

Figure S1. Crania of the Oligo-Miocene dromornithid *Dromornis murrayi* from Riversleigh, QM F57984, **A–H** and QM F57974, **I–P** depicted in photographs (**A**, **C**, **E**, **G**, **I**, **K**, **M**, **O**) and digital models (**B**, **D**, **F**, **H**, **J**, **L**, **N**, **P**). Digital models are derived from CT data used for the modelling of endocasts, and are arranged in the same approximate orientation as photo images of fossil specimens. **Views**, Right side lateral (**A**, **B**, **I**, **J**); rostral (**C**, **D**, **K**, **L**); caudal (**E**, **F**, **M**, **N**) and dorsal (**G**, **H**, **O**, **P**). Scale bars equal 40 mm.

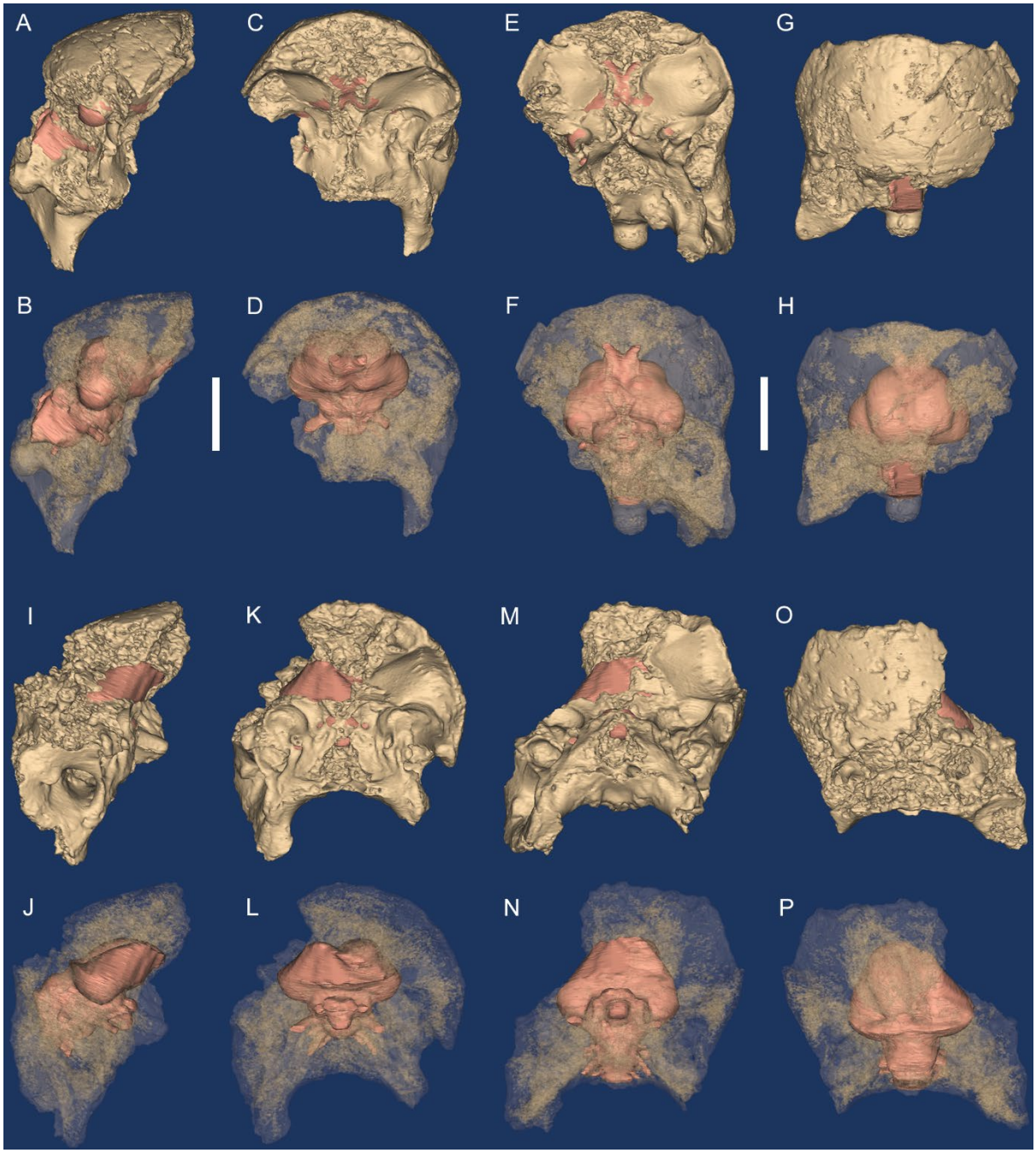

Figure S2. Digital reconstructions of crania for *Dromornis murrayi*: QM F57984 (**A–H)** and QM F57974 (**I–P)**. Crania are shown in solid (**A**, **C**, **E**, **G**, **I**, **K**, **M**, **O**) and transparent (**B**, **D**, **F**, **H**, **J**, **L**, **N**, **P**) views. Endocasts are shown within transparent crania and indicate location within the skull. Crania are orientated in approximate "alert posture" with respect to the horizontal positioning of the lateral semicircular duct of the vestibular organ (semicircular ducts + cochlea), as observed in *D. planei* and *I. woodburnei* (see Fig. S5, **4.1.4**). Trigeminal nerves (**V_1**, **V_2**, **V_3**) are truncated approximately where exiting the cranium. **Views**, Right side lateral (**A**, **B**, **I**, **J**); rostral (**C**, **D**, **K**, **L**); ventral (**E**, **F**, **M**, **N**) and dorsal (**G**, **H**, **O**, **P**). Scale bars equal 40 mm.

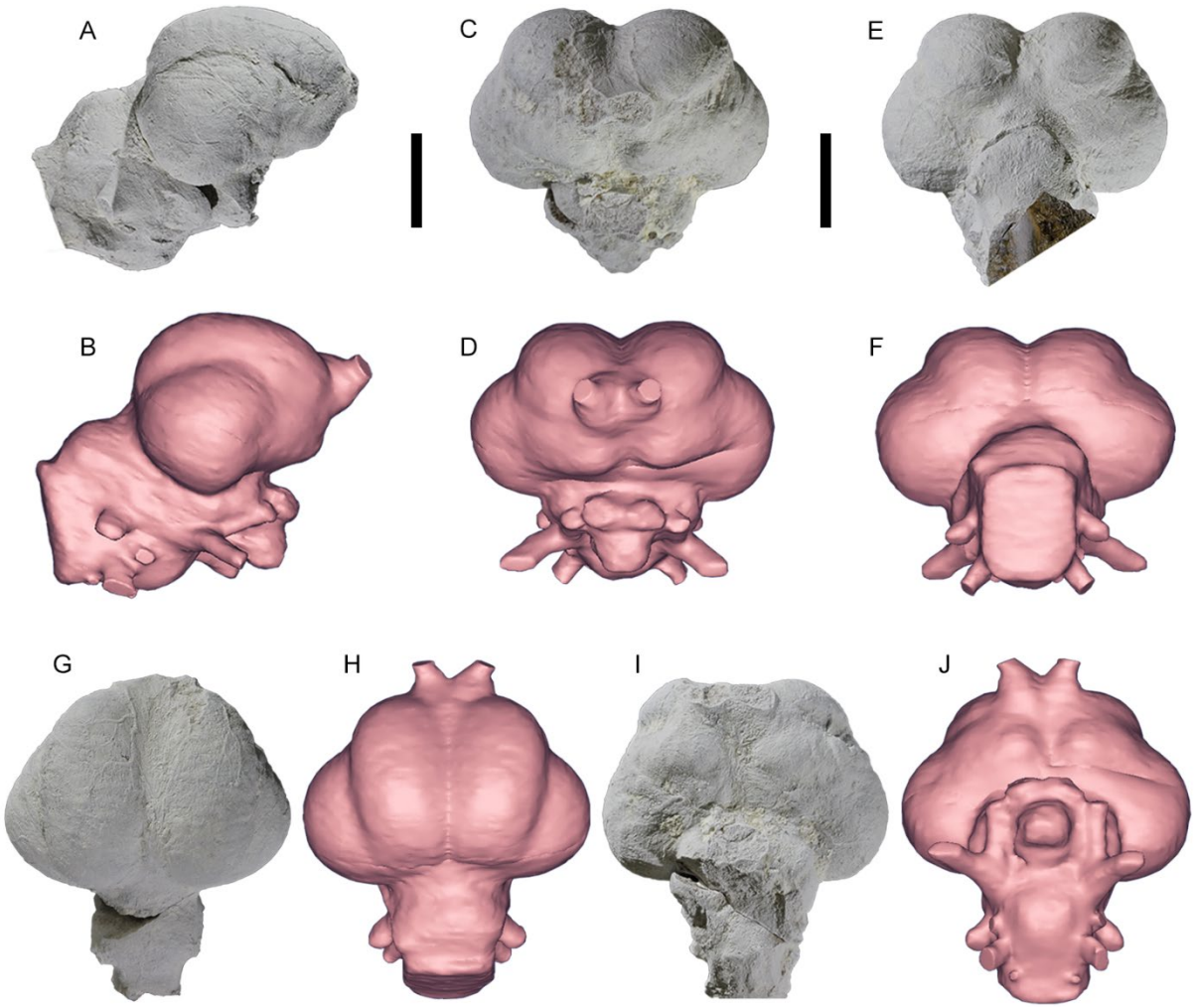

Figure S3. Fossil endocast of *Dromornis murrayi* QM F50412 (**A**, **C**, **E**, **G**, **I**; see **2.2**) whitened with ammonium chloride (NH_4Cl) compared to the digital endocast of *D. murrayi* (**B**, **D**, **F**, **H**, **J**) reconstructed from CT-data derived from the Riversleigh specimens QM F57984 and QM F57974 (see Figs. S1–S2, S9, **S2.2**). **Views**. Right side lateral (**A–B**); rostral (**C–D**); caudal (**E–F**); dorsal (**G–H**); ventral (**I–J**). Scale bars equal 20 mm.

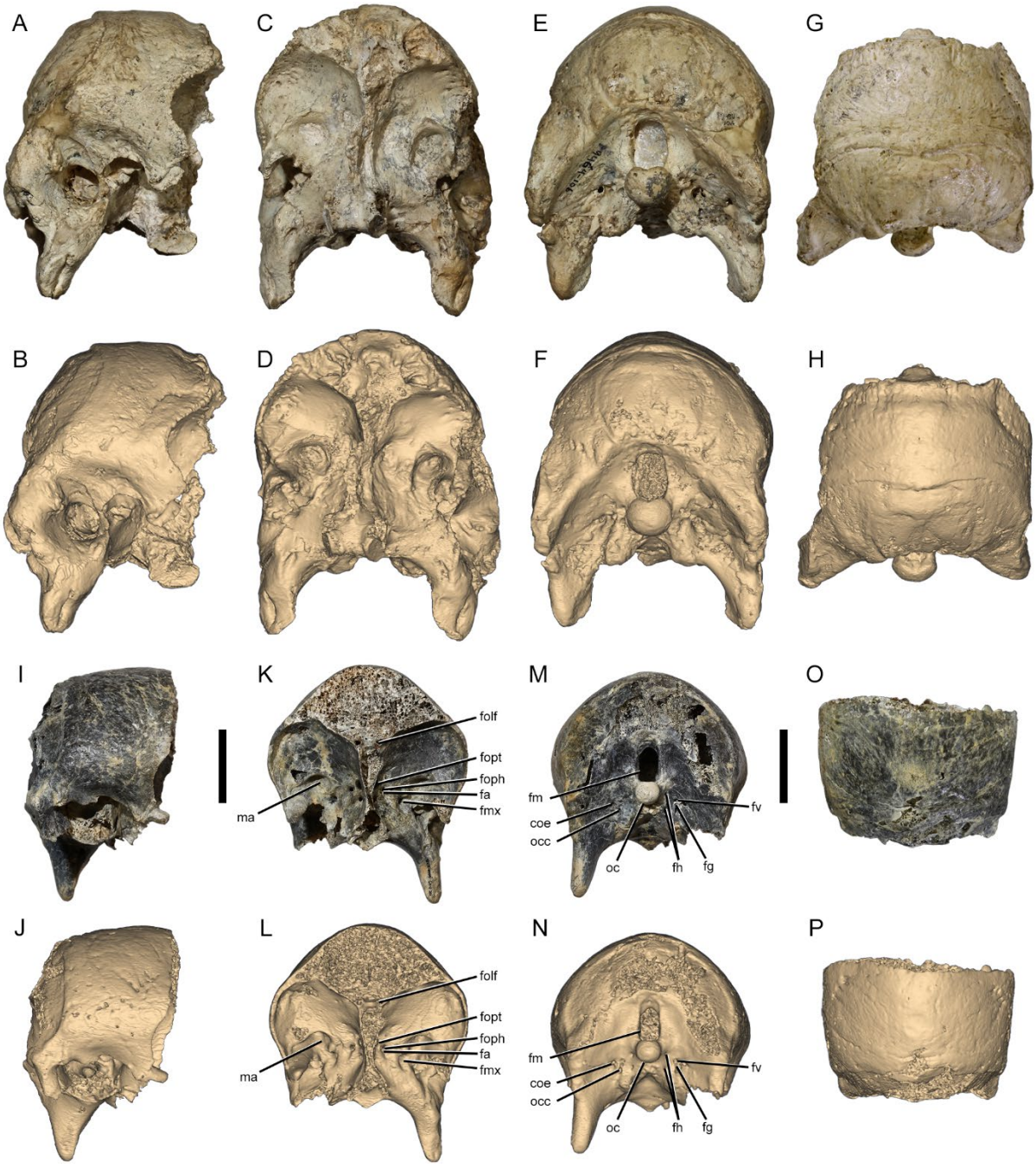

Figure S4. Photographs (**A**, **C**, **E**, **G**, **I**, **K**, **M**, **O**) and digital reconstructions (**B**, **D**, **F**, **H**, **J**, **L**, **N**, **P**) of crania from Middle Miocene dromornithid from Bullock Creek Local Fauna species. *Dromornis planei* NTM P9464-106 (**A–H**), and *Ilbandornis woodburnei* QVM:2000:GFV:20 (**I–P**). Digital models are derived from CT data used for the modelling of endocasts, and are arranged in the same approximate orientation as photo images of fossil specimens. **Views**, Right side lateral (**A**, **B**, **I**, **J**); rostral (**C**, **D**, **K**, **L**); caudal (**E**, **F**, **M**, **N**) and dorsal (**G**, **H**, **O**, **P**). **Abbreviations**. **coe**, canalis opthalmici externi for transmission of venae and arteria ophthalmica externa; **fa**, foramen n. abducentis (VI); **fg**, foramen n. glossopharyngeus (IX); **fh**, foramen n. hypoglossi (XII), **fm**, foramen magnum; **fmx**, foramen n. maxillomandibularis ($V_2 + V_3$); **folf**, foramen n. olfactorii (I); **foph**, foramen n. ophthalmici (V_1); **fopt**, foramen opticum (II); **fv**, foramen n. vagi (X); **ma**, insertion area for m. adductor mandibulae externus medialis et superficialis; **oc**, condylus occipitalis; **occ**, ostium canalis carotici (VII). Scale bars equal 40 mm.

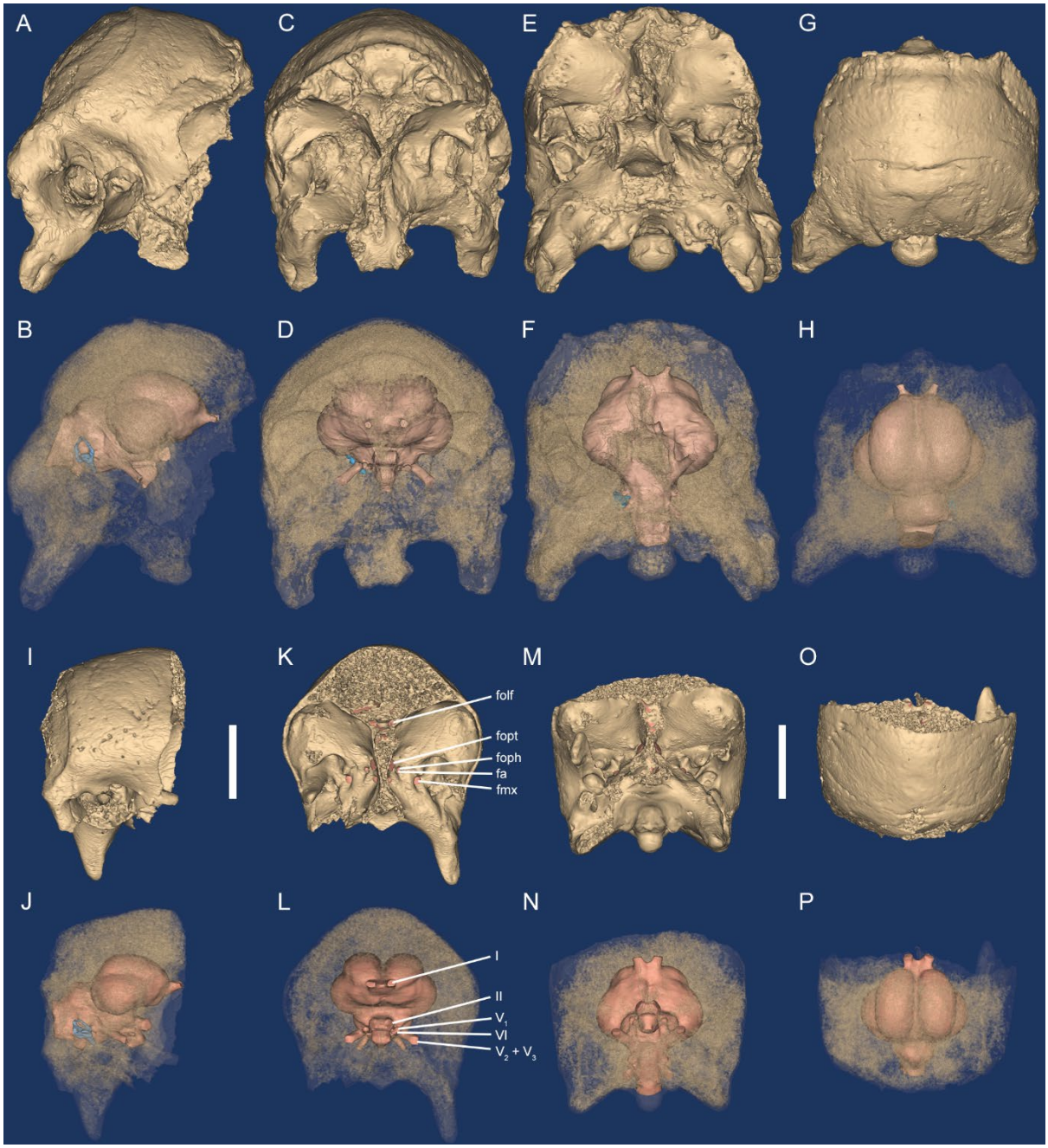

Figure S5. Digital reconstructions of crania from middle Miocene Bullock Creek Local Fauna species *Dromornis planei* (NTM P9464-106) (**A–H**), and *Ilbandornis woodburnei* (QVM:2000:GFV:20) (**I–P).** Crania are shown in solid (**A**, **C**, **E**, **G**, **I**, **K**, **M**, **O**) and transparent (**B**, **D**, **F**, **H**, **J**, **L**, **N**, **P**) views to reveal endocasts within the skull. Crania are orientated in approximate "alert posture" with respect to the horizontal positioning of the lateral semicircular duct of the vestibular organ (semicircular ducts + cochlea [blue]; see also **4.1.4**). Trigeminal nerves (**V_1**, **V_2**, **V_3**) are truncated approximately where exiting the cranium. **Views**, Right side lateral (**A**, **B**, **I**, **J**); rostral (**C**, **D**, **K**, **L**); ventral (**E**, **F**, **M**, **N**) and dorsal (**G**, **H**, **O**, **P**). **Abbreviations**. **fa**, foramen n. abducentis; **fmx**, foramen n. maxillomandibularis; **folf**, foramen n. olfactorii; **foph**, foramen n. ophthalmici; **fopt**, foramen opticum; **I**, olfactory nerve; **II**, optic nerve; **V_1**, ophthalmic nerve; **V_2**, maxillary nerve; **V_3**, mandibular nerve; **VI**, abducent nerve. Scale bars equal 40 mm.

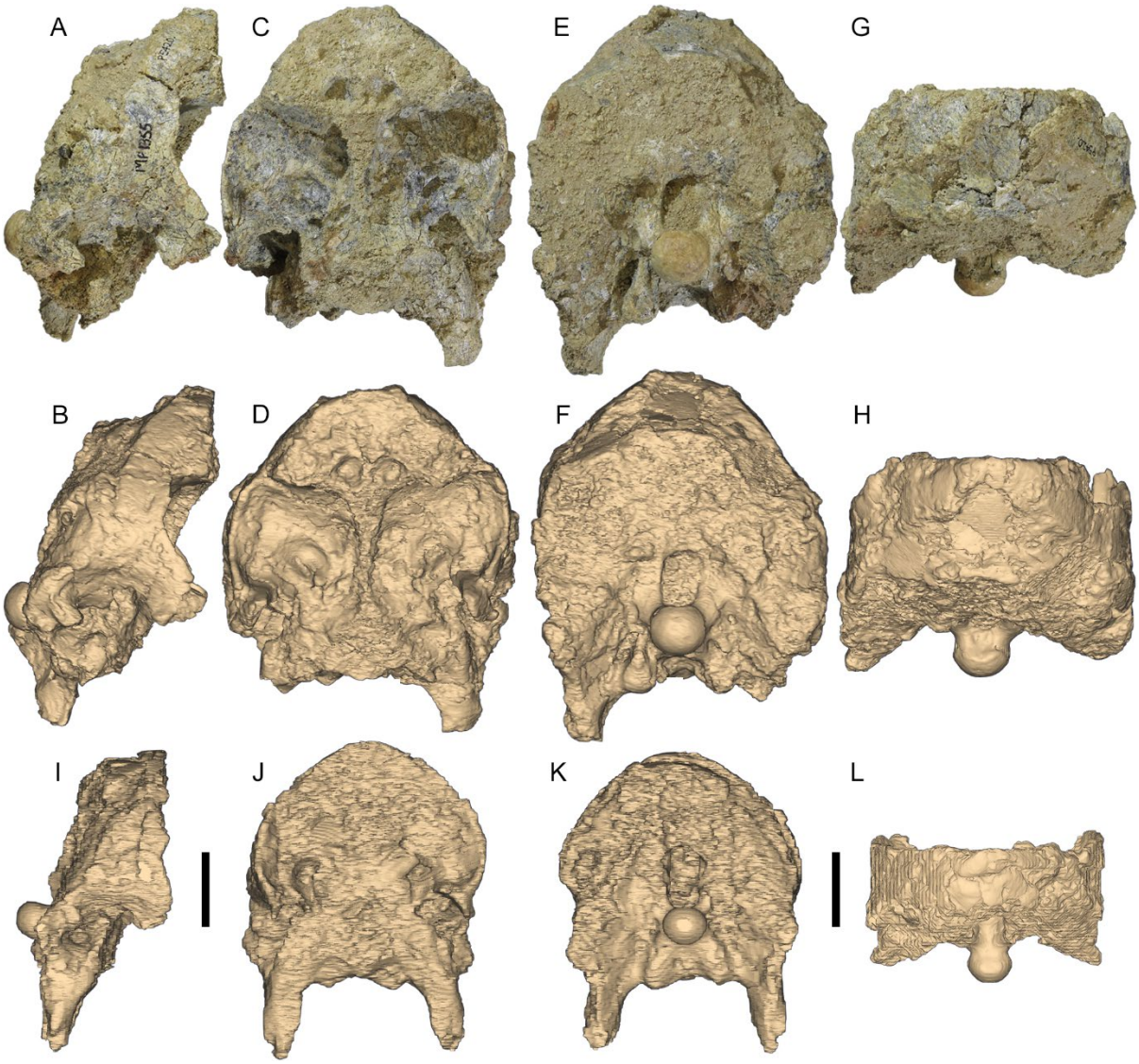

Figure S6. Photographs (**A**, **C**, **E**, **G**) and digital models (**B**, **D**, **F**, **H**, **I–L**) of crania of *Dromornis stirtoni* from the late Miocene Alcoota Local Fauna: NTM P5420 (**A–H**), and NTM P3250 (**I–L**). Digital models are derived from CT data used for the modelling of endocasts, and are arranged in the same approximate orientation as photo images of fossil specimens. **Views**, Right side lateral (**A**, **B**, **I**); rostral (**C**, **D**, **J**); caudal (**E**, **F**, **K**) and dorsal (**G**, **H**, **L**). Scale bars equal 40 mm.

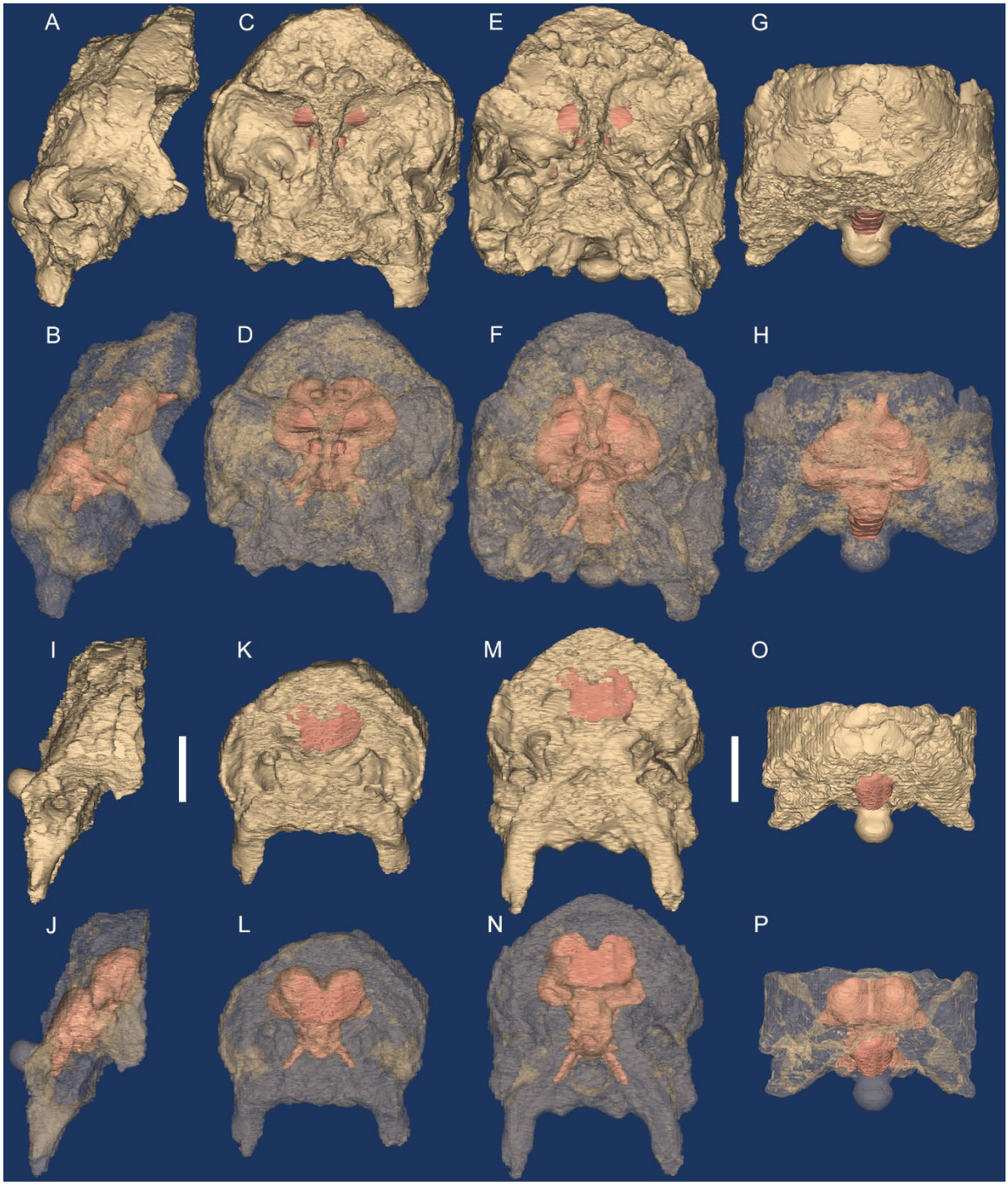

Figure S7. Digital models of crania shown in solid (**A**, **C**, **E**, **G**, **I**, **K**, **M**, **O**) and transparent revealing endocasts (**B**, **D**, **F**, **H**, **J**, **L**, **N**, **P**) views of *Dromornis stirtoni* from the late Miocene Alcoota Local Fauna: NTM P5420 (**A–H**), and NTM P3250 (**I–P**). Crania are orientated in approximate "alert posture" with respect to the horizontal positioning of the lateral semicircular duct of the vestibular organ (semicircular ducts + cochlea), as observed in *D. planei* and *I. woodburnei* (see Fig. S5, **4.1.4**). **Views**, Right side lateral (**A**, **B**, **I**, **J**); rostral (**C**, **D**, **K**, **L**); ventral (**E**, **F**, **M**, **N**) and dorsal (**G**, **H**, **O**, **P**). Scale bars equal 40 mm.

S2 Model reconstructions

S2.1 Two-dimensional (2D) model reconstructions–of the right hand side (RHS) lateral and rostral endocasts of *D. stirtoni*, were compiled in Adobe Photoshop v20.0 from 2D images of the endocast models for specimen NTM P5420 (Figs. S8D–S8E; hereafter *D. stirtoni*–1), and specimen NTM P3250 (Figs. S8G–S8H; hereafter *D. stirtoni*–2).

For the lateral RHS reconstruction (Fig. S8J), the endocast of the more gracile *D. stirtoni*–2 preserving the caudodorsal profiles of the wulst and cerebellum, was rescaled larger to fit the *D. stirtoni*–1 endocast, which preserved the rostro–caudal ventral profiles from the medial caudal diencephalon to the rostrodorsal wulst. Models were aligned at the ventral rhombencephalon by the caudoventral descending curve of the wulst through the caudal telencephalon in *D. stirtoni*–2, and the ventral curve of the caudal telencephalon in *D. stirtoni*–1. This feature, in the other dromornithid specimens assessed, tends to describe a somewhat continuous dorsoventral transition curve, which was replicated here. The so aligned *D. stirtoni* models were then overlain on the RHS lateral endocast of *D. planei* that was rescaled larger by approximately 8%, to approximate the size of the aligned specimens of *D. stirtoni*, so that differences in alignment of sections of the endocasts of the two species could be compared. The two species were aligned by fit to the rostrodorsal and caudodorsal eminence of the wulst, and the rostroventral eminence of the hypophysis, which in *D. stirtoni*–1 is reasonably well defined. With the alignment of these structures, the angle and extent of the preserved ramus of the maxillomandibular (V_2+V_3) nerves in *D. stirtoni*–1 is aligned with that of *D. planei*, and the angle of the rostrodorsal cerebellum surface matches that of *D. planei*, albeit located markedly more ventrally in *D. stirtoni*. Taken together, these morphological correlations likely represent the 'best fit' between specimens and thus show how endocasts of *D. stirtoni* and *D. planei* differed from each other (Fig. S8J).

For the rostral endocast reconstruction (Fig. S8K), the RHS rostral endocast morphology of *D. stirtoni*–1 and *D. stirtoni*–2 were used to align specimens, as both models appear to have suffered a measure of LHS rostroventrolateral distortion. As with the RHS lateral reconstruction, the more gracile rostral endocast of *D. stirtoni*–2 was rescaled larger to fit the RHS rostrodorsal eminence of the rostral RHS wulst in *D. stirtoni*–1. The eminence of the RHS caudal telencephalon and the ventral eminence of the rhombencephalon also aligns well between endocasts in this position. To enable comparison between the species, the rostral endocast of *D. planei* was then rescaled approximately 5% larger, aligned with the RHS eminence of the wulst, and with the RHS caudal telencephalon of the combined *D. stirtoni* specimens. With these features aligned, the position of the twin rostroventrolateral eminences of the rostral telencephalon, the vallecula telencephali (hereafter vallecula) transition zone, and the eminence of the chiasma opticum and hypophysis align well between species, but differences such as the more ventral location of the olfactory lobes in *D. planei* are apparent.

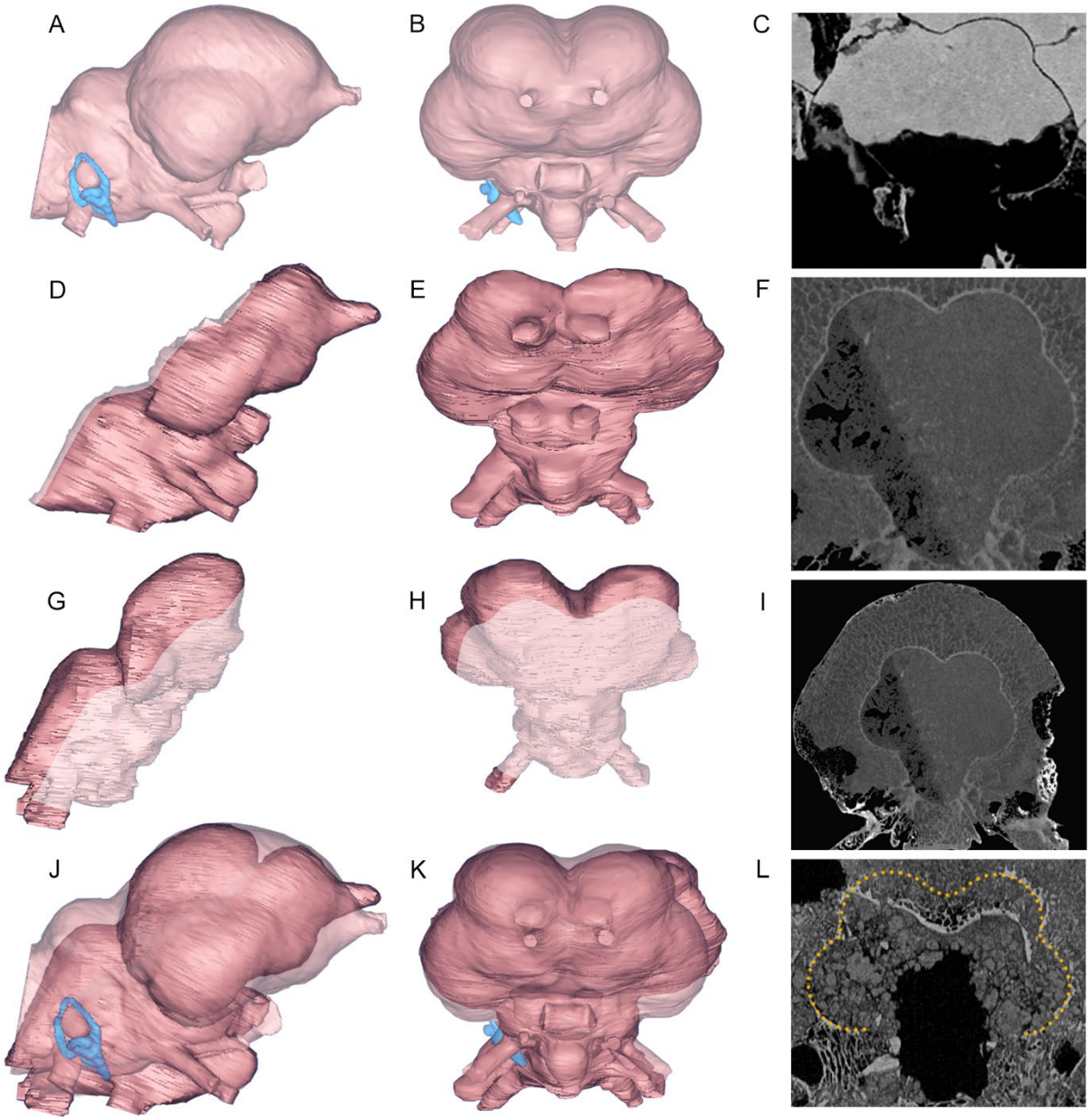

Figure S8. Endocast reconstructions in Right side lateral (**A**, **D**, **G**, **J**) and rostral (**B**, **E**, **H**, **K**) views for *Dromornis planei* NTM P9464-106 (**A**, **B**, opaque, 65%), *D. stirtoni* NTM P5420 (**D**, **E**) and *D. stirtoni* NTM P3250 (**G**, **H**), augmented with CT slice images viewed from the rostrocaudal aspect, showing the profile of the wulst and caudal telencephalon for *D. murrayi* QM F57984 (**C**), *D. planei* (**F**, **I**), and *D. stirtoni* NTM P3250 (**L**). **D** shows that the endocast of NTM P5420 is only complete in the rostro-caudoventral sections of the profile; in contrast **G** shows that the endocast of NTM P3250 preserves mainly the caudodorsal profile. Hypothesised form of the endocast for *Dromornis stirtoni* (**J**, **K**) from overlain partial endocasts of both **D+G** and **E+H** specimens respectively, with reference to that of *D. planei* (**A** and **B** respectively; opaque, 65%) to reveal differences between the two species (aligned by the fit of the rostrodorsal and caudodorsal eminence of the wulst, the rostroventral eminence of the hypophysis, and the maxillomandibular branch of the trigeminal nerve; see **S2.1** for details). **I**, CT-slice of complete dromornithid cranium to show the extent of the open-cell trabecular bone surrounding the endocranial cortical bone 'capsule' (see also **4.1.2**). **L**, a coronal CT-slice image derived from *D. stirtoni* (NTM P3250) showing displaced cortical bone of the endocranial capsule, and the presumed original endocranial profile in yellow stippled line. **Abbreviations**, **NTM**, Museum of Central Australia, Alice Springs, Northern Territory, Australia; **QM**, Queensland Museum, Brisbane, Queensland, Australia.

S2.2 Three-dimensional (3D) surface model reconstruction–a single endocast STL model was compiled from endocasts for the two specimens of *D. murrayi*, using Materialise 3-matic v10 software. As the specimen of *D. murrayi* QM F57984 (hereafter *D. murrayi*–1) preserves only the LHS dorsolateral endocast, and the specimen of *D. murrayi* QM F57974 (hereafter *D. murrayi*–2) preserves only the ventral endocast. The LHS dorsal endocast model of *D. murrayi*–1 was mirrored and positioned to form the RHS dorsolateral endocast surfaces, producing a complete dorsal surface model (Figs. S9 1–4). This reconstructed dorsal surface model was then positioned, with no re-scaling modification needed, upon the ventral endocast model of *D. murrayi*–2. The two surface models were then merged (Figs. S9 4–5), producing a single 3D STL endocast surface model (Fig. S9C).

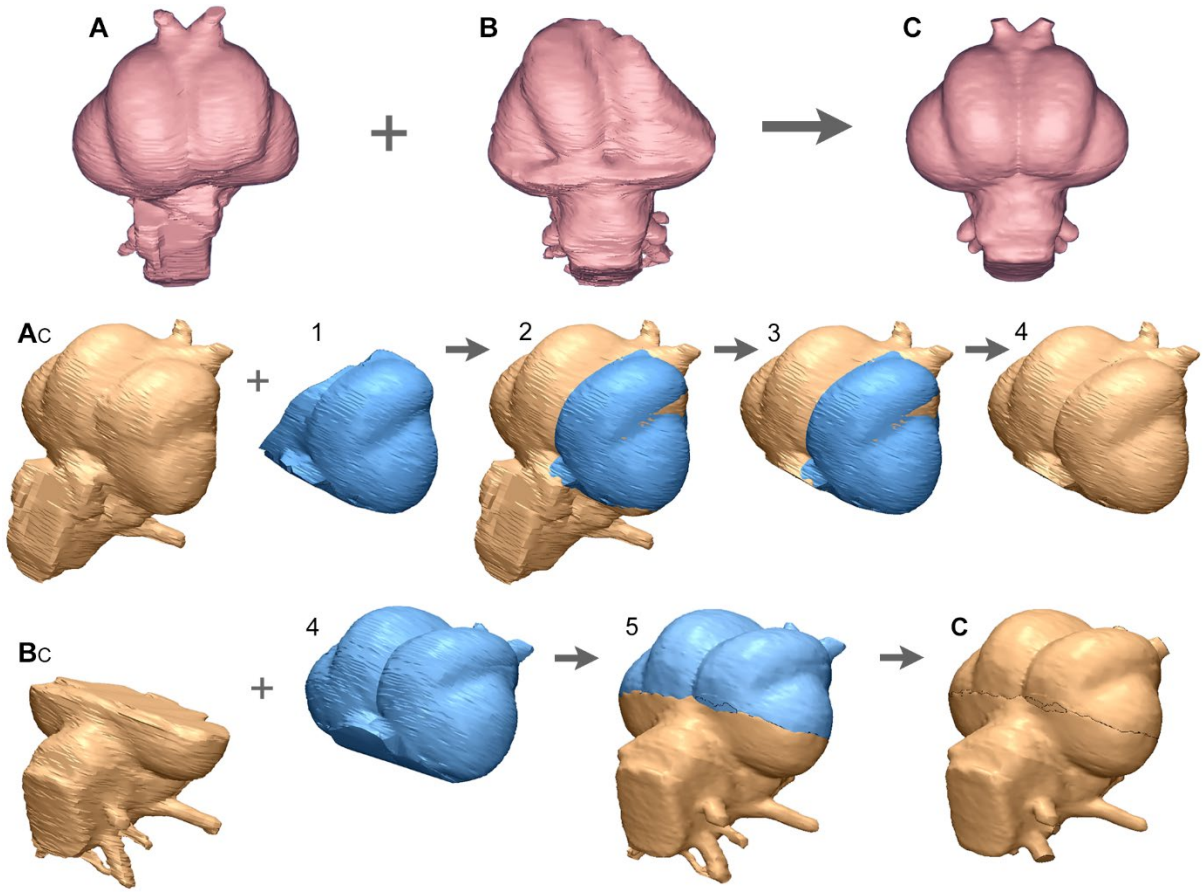

Figure S9. Reconstruction of the *Dromornis murrayi* endocast model. **A**, endocast of *D. murrayi* (QM F57984) preserving the dorsolateral left side endocast surfaces (see Figs. S2A–S2H); **A**C, caudolateral views of the workflow for reconstruction of the dorsal endocast (**4**) based on **A**; **B**, endocast of *D. murrayi* (QM F57974) preserving ventral surfaces (see Figs. S2I–S2P); **B**C, caudolateral views of the workflow for reconstruction of the complete endocast (**C**) based on **4**+**B**; **C**, complete reconstructed endocast of *D. murrayi* (QM F57984 + QM F57974). **Abbreviations**. Workflow **A**c: A copy of model (**A**) preserving the left side dorsolateral and caudodorsal surfaces was made, the left side dorsolateral surfaces were cropped out, mirrored, and flipped (**1**) to form the right side dorsolateral endocast surfaces. The model (**1**) was then (**2**) fitted to **A**, and ventral endocast surfaces were trimmed (**3**) from the model. The two models making up the dorsal surfaces were then merged to complete reconstruction of the dorsal endocast; Workflow **B**c: The damaged dorsal surfaces of the *D. murrayi* (QM F57974) endocast (**B**) were trimmed (**B**c), and the reconstructed dorsal endocast model (**4**) was fitted (**5**) to the resultant ventral endocast model (**Bc**), the complete reconstructed endocast model was then merged, trimmed and remeshed (**C** – see above).

S3 Landmark descriptions

S3.1 Fixed landmarks (n = 20)

S3.1.1 Lm 1 – Lm 20: Innervation module (Figs. 2, S11 [red dots]).

Innervation Lms were placed on nerve eminences truncated at the closest eminence (e.g. VIII; XII) or extension (e.g. I) of the nerve from the endocast surface. For all galloanseres, the ophthalmic (V_1) branch of the trigeminal (V) nerve, and abducent (VI) nerves were truncated where the nerves exit the os orbitosphenoidale, caudoventrolaterad of the foramen opticum (**fopt**, Figs. S4K–S4L, S5K), at the foramen n. ophthalmici (V_1 – **foph**, Figs. S4K–S4L, S5K) and foramen n. abducentis (VI – **fa**, Figs. S4K–S4L, S5K) respectively. The caudoventral transmission of the abducent (VI) nerves were segmented out of the rostroventral rhombencephalon, to facilitate full access to rhombencephalon surfaces. The remaining two eminences of the trigeminal (V) nerve complex, i.e., maxillary (V_2), and mandibular (V_3) nerves, were truncated approximately where exiting the cranium. The glossopharyngeal (IX) and vagus (X) nerves were truncated approximately upon bifurcation from the caudoventral proximal ganglia. In dromornithids, The divergence of the facial (VII), and vestibulocochlear (VIIIr + VIIIc) cranial nerves are distinct in the higher resolution *D. planei* CT data (e.g. **gv**, Fig. 3D), but in the lower resolution *D. murrayi* and *I. woodburnei* CT data, the divergence was indistinguishable (e.g. Figs. 3E, 3H, 3I, 3L). Thus, a single landmark was used to capture the eminence of the vestibular ganglion incorporating these three nerves (see Figs. 2B, S10A, S11A). Similarly, in dromornithids the hypoglossal (XIIr + XIIc) nerve complex was captured with a single Lm at the eminence of the hypoglossal (XII) ramus, on either side of the caudoventrolateral medulla oblongata (see **XII**, Fig. 2I). For all other galloanseres, the Lms were placed on the caudal ramus (XIIc) of the hypoglossal (XII) nerve (see also Figs. 4D, S10C, S11C, **3.1.9**).

Lm 1: Olfactory (I) nerve (LHS).

Lm 2: Olfactory (I) nerve (RHS).

Lm 3: Optic (II) nerve (LHS).

Lm 4: Optic (II) nerve (RHS).

Lm 5: Ophthalmic (V_1) nerve (LHS).

Lm 6: Ophthalmic (V_1) nerve (RHS).

Lm 7: Maxillary (V_2) nerve (LHS)

Lm 8: Maxillary (V_2) nerve (RHS)

Lm 9: Mandibular (V_3) nerve (LHS)

Lm 10: Mandibular (V_3) nerve (RHS)

Lm 11: Abducent (VI) nerve (LHS).

Lm 12: Abducent (VI) nerve (RHS).

Lm 13: Facial (VII) and Vestibulocochlear (VIIIr + VIIIc) nerve rami (LHS).

Lm 14: Facial (VII) and Vestibulocochlear (VIIIr + VIIIc) nerve rami (RHS).

Lm 15: Glossopharyngeal (IX) nerve (LHS).

Lm 16: Glossopharyngeal (IX) nerve (RHS).

Lm 17: Vagus (X) nerve (LHS).

Lm 18: Vagus (X) nerve (RHS).

Lm 19: Hypoglossal (XIIc) nerve, caudal ramus (LHS).

Lm 20: Hypoglossal (XIIc) nerve, caudal ramus (RHS).

S3.2 Semilandmark modules

IDAV Landmark v3.6 (53) software allows application of manipulatable rectangular 'patches' comprising Slms placed on grid junctions in any density configuration, i.e. 6 x 5 grid=30 Slms. Each corner of an initially rectangular Slm patch has a control point (CP) which is used to shift the patch into position, in-between each control point is mid curve control point (MCCP), and a centre control point (CCP) allowing additional patch manipulation (see Fig. S10). Control points (CPs) were used to anchor each Slm patch comprising the modular suite on morphologically appropriate endocast locations. Boundaries of anatomical zones were chosen which best followed the transition zone between endocast morphology, and patch boundaries were defined as sensibly as possible within these transition zones. Once appropriately applied, mid curve control points (MCCPs) and centre control points (CCPs) were made equidistant, ensuring consistent and comparable Slm locations within each module across all specimens. For Procrustes fitting (i.e. GPA; see **2.7.1)**, Slms on the patch periphery were treated as curve-sliding, and interior Slms were treated as surface-sliding Slms.

Descriptions for rostral telencephalon modules (see below) pertain to all specimens excluding dromornithids, as eminences of the dromornithid rostral telencephalon are either entirely masked by the wulst, and only present external morphology rostrally, or are entirely absent from the surface profile of dromornithid endocasts (see **3.2.1**). Rostral telencephalon modules were applied to dromornithid endocasts to ensure Modular Lm suite continuity across all specimens for GPA procedures, but formed no part of subsequent assessments.

S3.2.1 Curve and surface sliding Slms (n = 460; Figs. 2, S11 [green dots]); the number of Slms per module are indicated in parenthesis (n = xx).

S3.2.1.1 Slm 21 – Slm 65: Wulst module LHS (n = 45); the rostral MCCPs form the most rostrodorsal eminence of the wulst, similarly the caudal CCPs are placed at the most caudodorsal eminence. The rostrolateral MCCPs are placed in close proximity with the shared rostrodorsal and caudodorsal CPs of the telencephalon modules (see below), allowing for the rostrolateral CPs to be placed equidistant with the rostrodorsal MCCPs and the rostromedial CPs. The caudolateral CPs are placed equidistant with the caudodorsal MCCPs so that the caudolateral curves describe the vallecula (**va**, Figs. 3B–3C, 4C) transition zone between the caudolateral wulst and the dorsolateral caudal telencephalon. The caudodorsal MCCPs are placed equidistant with the caudodorsal CPs so that the

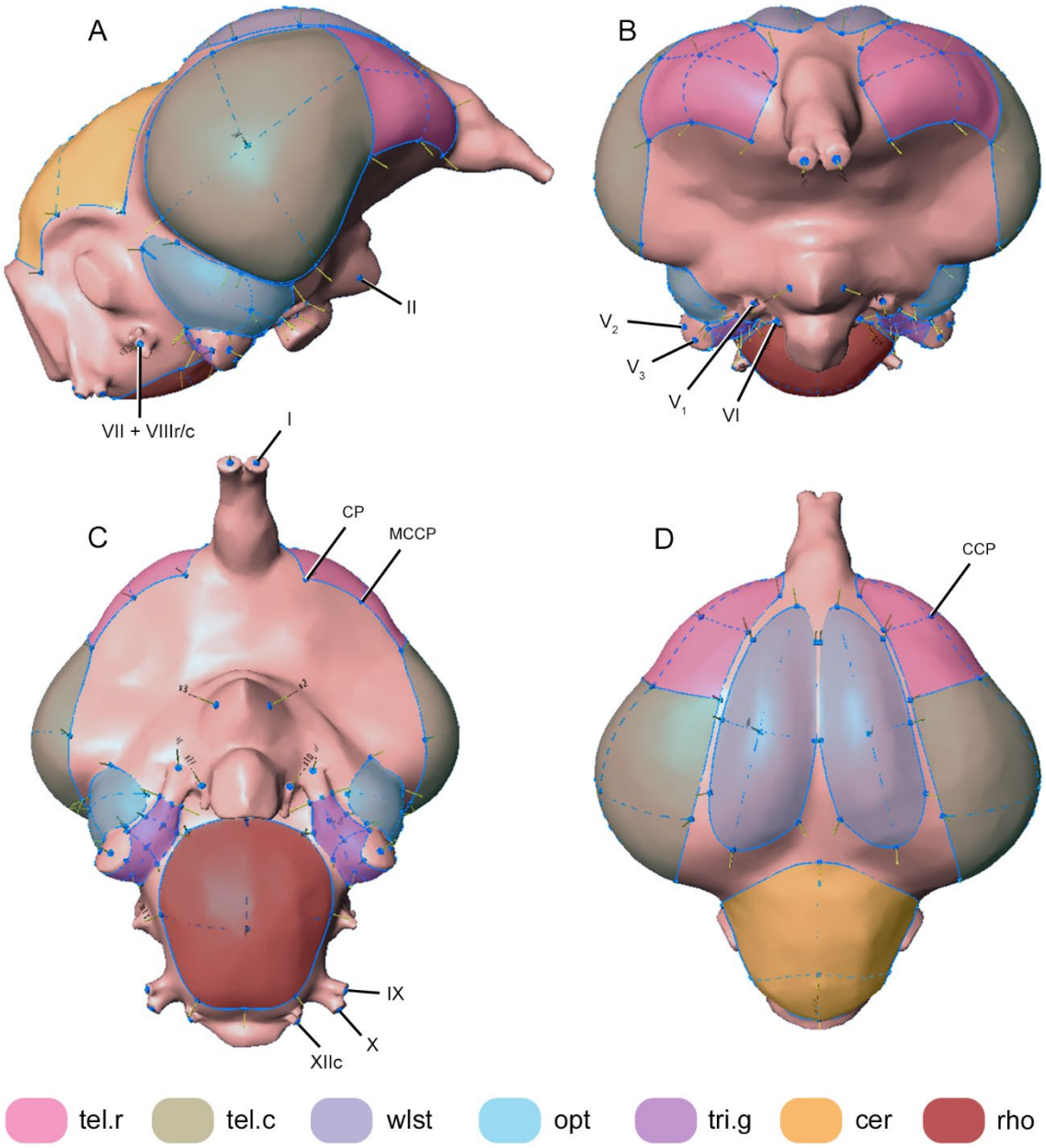

Figure S10. Landmark and semilandmark modules used to capture endocast morphology, mapped onto the endocast of *Anhima cornuta* (MV B12574) and shaded to facilitate anatomical identification (see also Fig. S11 below). **Views**: **A**, lateral right side; **B**, rostral; **C**, ventral; **D**, dorsal. **Abbreviations**, **cer**, cerebellum; **CP**, control point; **CCP**, centre patch control point; **MCCP**, mid-curve control point; **opt**, optic lobe; **rho**, rhombencephalon; **tel.c**, caudal telencephalon; **tel.r**, rostral telencephalon; **tri.g**, trigeminal ganglion; **wlst**, wulst; **I**, left side olfactory nerve; **II**, right side optic nerve; **V_1**, ophthalmic nerve; **V_2**, maxillary nerve; **V_3**, mandibular nerve; **VI**, abducent nerve; **VII + VIIIr/c**, rami of the facial (VII) nerve, and the rostral (VIIIr) and caudal (VIIIc) vestibulocochlear nerves; **IX**, glossopharyngeal nerve; **X**, vagus nerve; **XIIc**, caudal ramus of the hypoglossal nerve (see **3.1.9**, **S3.1.1**). Endocasts are not to scale.

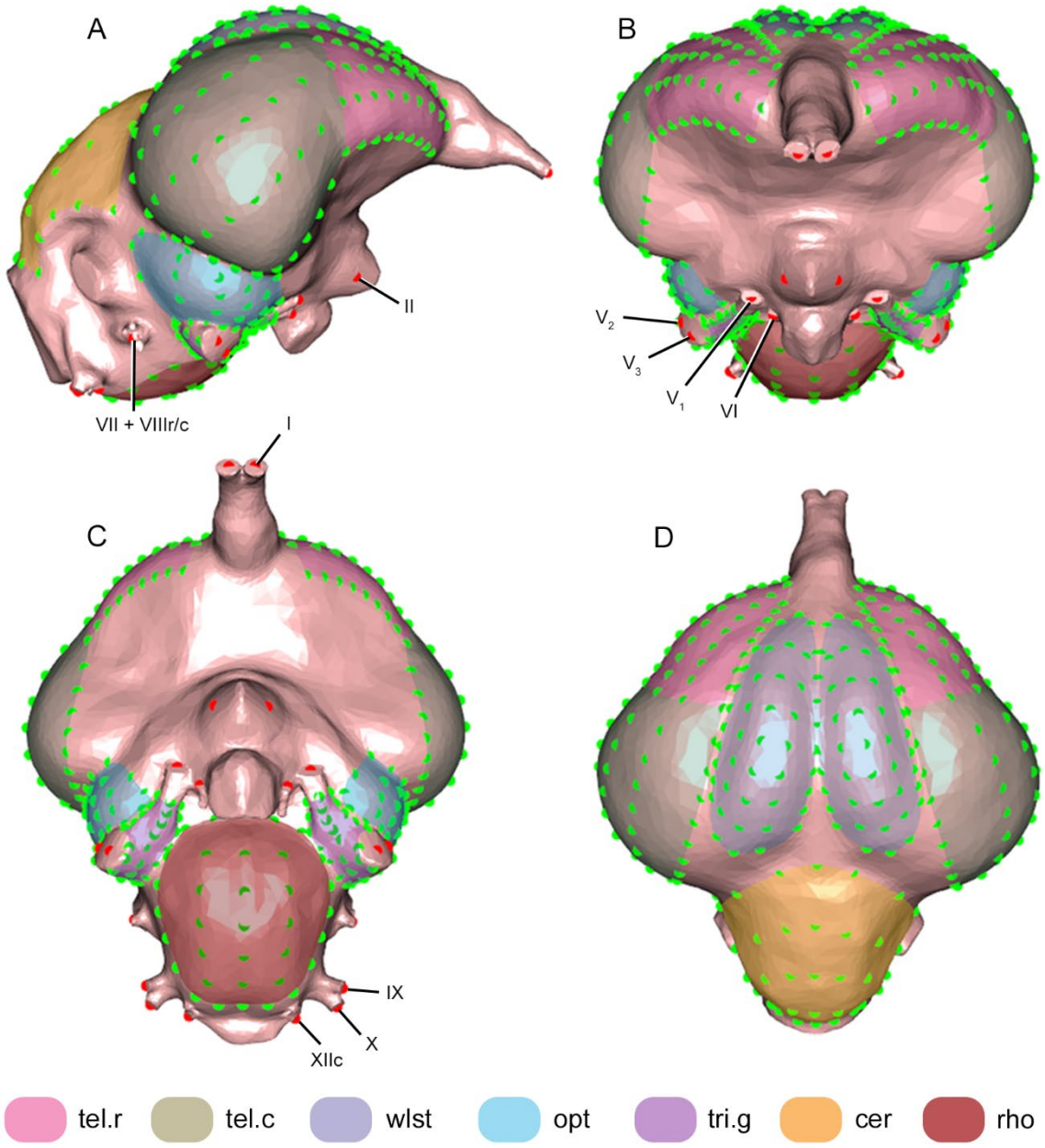

Figure S11. Brain surface Slm modules (green dots) and innervation Lm module (red dots), mapped onto the endocast of *Anhima cornuta* (MV B12574) and shaded to facilitate anatomical identification (see also Fig. S10 above). **Views**: **A**, lateral right side; **B**, rostral; **C**, ventral; **D**, dorsal. **Abbreviations**, **cer**, cerebellum; **Lm**, landmark; **opt**, optic lobe; **rho**, rhombencephalon; **Slm**, semilandmark; **tel.c**, caudal telencephalon; **tel.r**, rostral telencephalon; **tri.g**, trigeminal ganglion; **wlst**, wulst; **I**, left side olfactory nerve; **II**, right side optic nerve; **V_1**, ophthalmic nerve; **V_2**, maxillary nerve; **V_3**, mandibular nerve; **VI**, abducent nerve; **VII + VIIIr/c**, rami of the facial (VII) nerve, and the rostral (VIIIr) and caudal (VIIIc) vestibulocochlear nerves; **IX**, glossopharyngeal nerve; **X**, vagus nerve; **XIIc**, caudal ramus of the hypoglossal nerve (see **3.1.9**, **S3.1.1**). Endocasts are not to scale.

medial curves describe the fissura interhemispherica (**fi**, Figs. 3B, 4C) transition zones between wulst modules. The CCPs are then made equidistant mediolaterally between the caudolateral and caudodorsal MCCPs, and equidistant between the rostrodorsal MCCPs and caudodorsal MCCPs.

S3.2.1.2 Slm 66 – Slm 110: Wulst module RHS (n = 45); see Wulst module LHS.

S3.2.1.3 Slm 111 – Slm 155: Rostral telencephalon module LHS (n = 45); the most rostral ventrolateral eminence of the telencephalon, forms the location of the rostrolateral CPs for the rostral telencephalon modules. The ventrolateral curve of the rostral telencephalon modules closely corresponds with the descending dorsolateral curve of the cerebrum fovea limbica (**cfl**, Figs. 3A, 4A) transition. The caudoventral CPs terminate at the dorsoventral traversal of the medial cerebral artery (**acm**, Figs. 4B, 4D) across the telencephalic hemisphere. The rostrocaudal boundary between the rostral and caudal telencephalon modules (see below) is defined by the dorsoventral traversal of the medial cerebral artery. The dorsomedial CPs are situated at the point of transition into the rostral wulst, the MCCPs are placed equidistantly between the rostral dorsolateral CPs, and situated so as to track the medial transition zone of the rostral telencephalon into the fissura interhemispherica (**fi**, Figs. 3B, 4C). The caudodorsal CPs are situated equidistant with respect to the dorsomedial CPs and the rostrolateral CPs, with the MCCPs situated equidistant between the former, and located so as to align the dorsolateral modular curve with the dorsolateral vallecula transition zone between the rostral telencephalon and the wulst. The caudal MCCPs between the caudodorsal CPs and the caudoventral CPs are made parallel and equidistant between CCPs and MCCPs.

S3.2.1.4 Slm 156 – Slm 200: Rostral telencephalon module RHS (n = 45); see Rostral telencephalon module LHS

S3.2.1.5 Slm 201 – Slm 245: Caudal telencephalon module LHS (n = 45); the dorsoventral boundary between the rostral telencephalon module and the caudal telencephalon module share five Slms that are located identically, allowing for the full Slm complement of the caudal and rostral telencephalon modules to be subset and analysed individually, or combined as a single total cerebrum module. The rostrodorsal and rostroventral CPs of the caudal telencephalon modules occupy the same locations as the rostral telencephalon modules caudodorsal and caudoventral CPs respectively. The caudodorsal CPs of the caudal telencephalon module are situated at the transition zone of the dorsolateral cerebellum and the caudoventral eminence of the wulst (see above). The MCCPs are made equidistant, and situated to align the curve appropriately with the rostrocaudal vallecula transition zone of the dorsal caudal telencephalon into the wulst. The rostral and caudal MCCPs and ventrolateral CPs are equidistantly located so as to align the curve in the transition zone between the ventrolateral caudal telencephalon, and the dorsolateral optic lobe in the fissura subhemispherica (**fs**, Figs. 3B, 4B) zone. The CCPs are then made dorsoventrally and rostrocaudally equidistant.

S3.2.1.6 Slm 246 – Slm 290: Caudal telencephalon module RHS (n = 45); see Caudal telencephalon module LHS.

S3.2.1.7 Slm 291 – Slm 320: Optic lobe module LHS (n = 30); the large trigeminal ganglion incorporating the three branches of the 5th cranial nerve (V; see **S3.1.1** above), inserting on the ventral surface of the optic lobe, occupies a proportion of the ventromedial optic lobe surface (see **tri.g**, Figs. 3D, 4A, 4D). Thus, optic lobe modules were arranged so as to define the margin of the trigeminal ganglion interface with the dorsolateral optic lobe (Figs. 2I, S10C, S11C). Rostral MCCPs and dorsal and ventral CPs are placed where the swell of the optic lobe transitions into the caudolateral chiasma opticum and tractus opticus structures. Caudal CPs are placed where the optic lobe terminates into the dorsomedial pons and medulla oblongata structures (metencephalon), comprising the mediolateral rhombencephalon transition. Boundary curves are situated so that the dorsal curve describes the transition from the optic lobe into the ventrolateral caudal telencephalon at the fissura subhemispherica zone, and the ventral curve follows the transition from the dorsal optic lobe into the ventromediolateral rhombencephalon. MCCPs and CCPs are then made equidistant.

S3.2.1.8 Slm 321 – Slm 350: Optic lobe module RHS (n = 30); See Optic lobe module LHS.

S3.2.1.9 Slm 351 – Slm 380: Trigeminal ganglion module LHS (n = 30); the trigeminal ganglion module is constructed of two patches that are merged after fitment. The first patch captures the ophthalmic (V_1) nerve's rostral eminence, and the second, the eminence of the maxillomandibular (V_2 +V_3) branch. For the rostral ophthalmic (V_1) patch, the rostrolateral CPs are placed in rostral proximity from where the ophthalmic nerve (V_1) eminence separates from the surface of the rhombencephalon (see below) and optic lobe respectively. The dorsolateral curve describes the transition zone between the trigeminal ganglion and the ventral optic lobe, and the caudal CP is placed in the junction at the eminence of the maxillomandibular (V_2 +V_3) branch. The medial CP is aligned with the transition between the trigeminal ganglion and the rhombencephalon, and the curve follows the transition zone rostroventrally. The second (caudal) patch describes the maxillomandibular (V_2 +V_3) branch, where the dorsolateral CP is placed in the junction at the eminence of the maxillomandibular (V_2 +V_3) nerve, and shares the location of the rostral (V_1) patch CP. The dorsolateral curve of the caudal patch describes the ventromedial margin of the truncated face of the maxillomandibular (V_2 +V_3) nerve eminence, to a point approximately level with the rostral junction CP. The caudal transmission of the patch curve follows the most caudal eminence of the trigeminal ganglion, to meet the transition into the medulla oblongata, and returns following the transition from the ventral rhombencephalon. MCCPs and CCPs are then made equidistant, and the two CPs and MCCPs forming the medial junction between the two patches are merged, forming one Slm module.

S3.2.1.10 Slm 381 – Slm 410: Trigeminal ganglion module RHS (n = 30). See Trigeminal ganglion module LHS.

S3.2.1.11 Slm 411 – Slm 445: Cerebellum module (n = 35); the rostromedial MCCP forms the most dorsal rostromedial eminence of the cerebellum module and is placed approximately in the area of the glandula pinealis (**gp**, Figs. 3A, 3C, 4C). The caudal MCCP is placed at the most caudodorsal eminence of the cerebellum, where the medulla spinalis exits at the foramen magnum.

The caudolateral CPs are placed at the most ventrolateral eminences of the cerebellum, at the transition of the auricula cerebelli into the dorsomediolateral medulla oblongata/rhombencephalon complex. The MCCPs are made equidistant with the rostromedial and rostrosagittal MCCPs, so that the ascending lateral curves describe the transition zones between the lateral optic lobe and the caudal telencephalon, in the vicinity of the caudal cerebrum pars occipitalis dorsally, and ventrally in the area of the mediolateral rhombencephalon complex. The CCP is then made mediolaterally and rostrocaudally equidistant.

S3.2.1.12 Slm 446 – Slm 480: Rhombencephalon module (n = 35); the rostral MCCP forms the most rostroventromedial point of the rhombencephalon module, and is placed in the transition zone between the rhombencephalon and hypophysis (**h**, Figs. 3A, 4A). The caudal MCCP is placed where the medulla oblongata transitions into the medulla spinalis. The rostrolateral CPs are placed in the vicinity of the rostroventral optic lobe CPs (see above). The caudolateral CPs are placed at the point where the medulla oblongata widens mediolaterally, forming a shelf between the mediolateral pons and the caudal medulla spinalis, so that the medial curves describe the transition zones between the ventrolateral optic lobe and the dorsolateral rhombencephalon. The lateral MCCPs are then made equidistant with the lateral rostrocaudal CPs, and the CCP is made equidistant with the rostrocaudal and ventrolateral MCCPs.

S4 Endocast comparisons between species of dromornithid

Modular shape distinctions as described by 3D modular shape variation plots (see Fig. 5, **2.7.2**), accompanied by size-standardised Measurement (see Figs. S12–S13, Table 1B), and Surface Area (see Fig. S14, Table 1D) log shape ratio results, are presented below with respect to endocast morphological differences between species of dromornithid. [Note: as dromornithid rostral telencephalon structures appear entirely masked by the dorsal wulst (see **3.2.1**), landmarked comparisons of these structures were not practicable].

S4.1 *Dromornis* species–*D. murrayi* compared with *D. planei*

We first compare *Dromornis murrayi* and *D. planei* to assess the morphological transition in the genus from the late Oligocene through the middle Miocene periods.

S4.1.1 Wulst modules–3D modular shape variation plots of the wulst of *D. murrayi* and *D. planei* (Fig. 5D), show that between the ~20 Ma *D. murrayi* and the ~12 Ma *D. planei*, there occurred a rostrodorsal hypertrophy of the wulst that has largely masked the full extent of the olfactory bulb still visible in *D. murrayi* (Fig. 3E), i.e., olfactory morphology becomes less apparent in the younger *D. planei* (Fig. 3A). There is no evidence to suggest the olfactory bulb has reduced in relative size over time between these species, as the extent of the olfactory bulb of *D. planei* is visible from the ventral aspect (Fig. 3D), and apparently increased in mediolateral width relative to that observed in *D. murrayi* (Fig. 3H). Furthermore, the rostrolateral profile of the olfactory zone in *D. planei* (Fig. 3A), suggests the olfactory bulb of *D. planei* is minimally of comparable volume to that of *D. murrayi*, and

has likely been incorporated within the rostral hypertrophy of the wulst, masking it from dorsal view in *D. planei*.

Not only has the hypertrophy of the wulst markedly increased the rostrodorsal eminence of the structures in *D. planei* compared with *D. murrayi* (Figs. 5D, 5F), but results for Measurement data show length (0.415 vs 0.362, respectively; Table 1B), and width (0.122 vs 0.056, respectively; Table 1B) log shape ratios of the wulst has increased as well (Fig. S12). These trends are well described by results for Modular Surface Area data, where wulst log shape ratios for *D. planei* and *D. murrayi* reveal an increase in surface area log shape ratios between them (0.720 vs 0.655, respectively; Fig. S14, Table 1D). In addition, mediolateral hypertrophy of the wulst in *D. planei* has shifted the lateral margins, displacing the vallecula transition zones between the dorsolateral wulst, and the dorsal caudal telencephalon somewhat ventrolaterally, in comparison with that of *D. murrayi* (Fig. 5F). Notably, the ventrolateral shifting of the vallecula transition zones in *D. planei* are more pronounced in the dorsal caudolateral regions of the endocast. The caudolateral wulst margins appear to have shifted laterally to a greater degree, with respect to the sagittal fissura interhemispherica zone, than occurred in the rostral regions of the endocast between specimens (Figs. 5D, 5F).

S4.1.2 Caudal telencephalon modules–the overall hypertrophy of the wulst in *D. planei* compared with that of *D. murrayi*, is associated with a compensatory ventral rotation of the dorsolateral surface of the caudal telencephalon. Resulting in the dorsolateral margins, defined by the vallecula, of the caudal telencephalon in *D. planei* becoming more ventrally orientated than in *D. murrayi* (Fig. 5F). The ventrolateral shifting of the vallecula transition zones, has translated to a positional displacement of the most ventral eminence of the caudal telencephalon in the area of the fissura subhemispherica too. Yet a similar dorsoventral and rostrocaudal caudal telencephalon shape is maintained in both specimens (Fig. 5F). However, while a similar shape has been preserved, there has occurred a dorsomediolateral reduction in the dorsoventral ‘profile’ of the caudal telencephalon in *D. planei*. Results for Measurement data show that the ventral rotation of these structures in *D. planei*, have resulted in an overall reduction in the dorsoventral width log shape ratio with respect to *D. murrayi* (0.193 vs 0.229, respectively; Fig. S12, Table 1B). Along with a commensurate reduction in rostrocaudal length log shape ratio for *D. planei* (0.281 vs 0.289, respectively; Fig. S12, Table 1B), but to a lesser degree (see Fig. 5F). Results for Surface Area data are consistent with these trends, and show that *D. murrayi* has a larger surface area log shape ratio than that of *D. planei* (0.608 vs 0.566, respectively; Fig. S14, Table 1D).

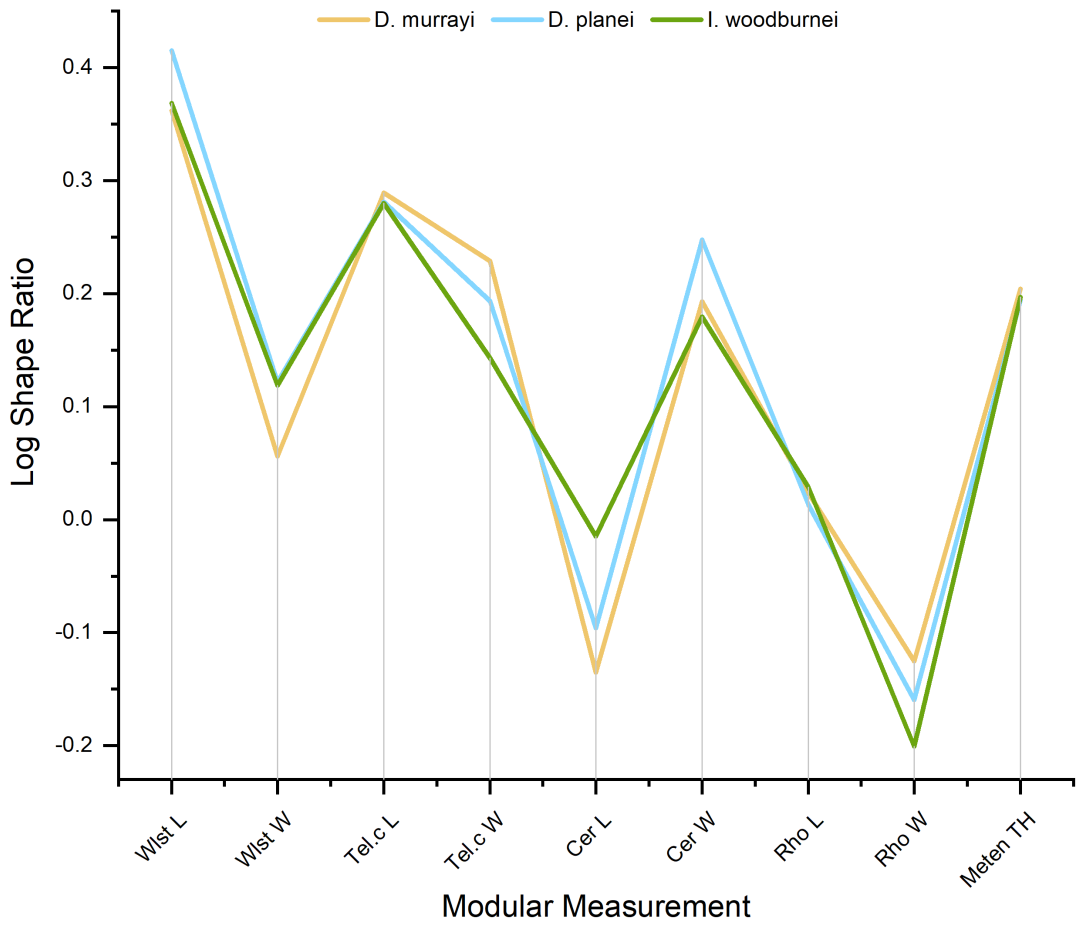

Figure S12. Mean Measurement log shape ratios plot for species of dromornithid. Size-standardised log shape ratio data were computed by the log shape method, where species Measurement values were divided by species endocast volume values and $\log_{10}$ transformed (see **2.6.2**, Table 1B). **Abbreviations**; **Cer L**, cerebellum length; **Cer W**, cerebellum width; **D. murrayi**; *Dromornis murrayi* reconstruction (QM F57984 + QM F57974); **D. planei**; *Dromornis planei* (NTM P9464-106); **I. woodburnei**; *Ilbandornis woodburnei* (QVM:2000:GFV:20); **Meten TH**, metencephalon total height; **Rho L**, rhombencephalon length; **Rho W**, rhombencephalon width; **Tel.c L**, caudal telencephalon length; **Tel.c W**, caudal telencephalon width; **Wlst L**, wulst length; **Wlst W**, wulst width.

S4.1.3 Cerebellum module–3D modular shape variation plots of the cerebellum of *D. murrayi* and *D. planei* (Fig. 5F), are suggestive of a rostrodorsal hypertrophy of this structure in *D. planei*. These observations are supported by results for Measurement data, which show an increase in length (-0.135 vs -0.096, respectively; Fig. S12, Table 1B) and width log shape ratios (0.193 vs 0.248, respectively; Fig. S12, Table 1B) between species. These differences are likely describing the increase in cerebellum rostrodorsal height between *D. murrayi* and *D. planei*, as the Measurement data captures the individual vectors between Slms describing the directional curve over a modular structure (see Fig. 2F, **2.6.2**), these data are likely representative of the transition to a higher dorsal cerebellum surface in *D. planei*, relative to ventrolateral boundaries. Results for Surface Area data supports this, and show that *D. murrayi* has a somewhat smaller Surface Area log shape ratio than *D. planei* (0.355 vs 0.365, respectively; Fig S14, Table 1D).

S4.1.4 Rhombencephalon module–results for Measurement data show that *D. murrayi* has a slightly larger overall length log shape ratio than *D. planei* (0.024 vs 0.013, respectively; Fig. S12, Table 1B). Similarly, the width log shape ratio for *D. murrayi* is larger compared with that of *D. planei* (-0.125 vs -0.159, respectively; Fig. S12, Table 1B). Results for Surface Area data show that *D. murrayi* has a smaller Surface Area log shape ratio than *D. planei* (0.119 vs 0.221, respectively; Fig. S14, Table 1D). The ventral position of the rhombencephalon relative to dorsal morphology of the endocast, has apparently shifted dorsally during this period as well (Fig. 5F). While it could be argued that the accurate placement of the rhombencephalon structure in *D. murrayi* may be compromised due to the endocast being a reconstruction of two specimens, and thus may not be representative of the taxon; the ventral regions of the *D. murrayi* reconstruction, including the cerebellum and the rhombencephalon, were sourced from a single specimen, and only the RHS rostrodorsal surface of the endocast was reconstructed (see Fig. S9, and **S2.2** above). Furthermore, the positioning of the lateral boundaries of the cerebellum (Figs. 5E–5F) imply they are comparatively orientated, and that the more ventral location of the rhombencephalon in *D. murrayi* (Fig. 5F), represents an accurate morphological state for the taxon. In support of this, the form of the rhombencephalon preserved in the fossil endocast of *D. murrayi* (Fig. S3A), suggests the rhombencephalon in *D. murrayi* does project further ventrally than it does in *D. planei*. Therefore, the reconstructed endocast model of *D. murrayi* (Figs. 3E, S3B) likely represents the form of the rhombencephalon accurately. Assuming this is so, then the rhombencephalon surface became displaced dorsally in *D. planei* relative to *D. murrayi*, and the mediolateral and rostrocaudal profile of the rhombencephalon was reduced in *D. planei* (Fig. 5F). This suggests that the rhombencephalon develops an overall ‘flatter’ mediolateral and rostrocaudal shape, between the late Oligocene and the middle Miocene.

Morphological differences in the dorsal cerebellum and ventral rhombencephalon described above, are not well reflected in Measurement log shape ratios for the total height of the metencephalon (cerebellum + pons, see **2.6.2**), between *D. murrayi* and *D. planei* (0.204 vs 0.194, respectively; Fig. S12, Table 1B), where differences between species are not substantial, and is likely a reflection of the more hypertrophied state of the rostrodorsal cerebellum in *D. planei*, accommodating for the ‘flatter’ rhombencephalon profile in the species. Measurement log shape ratios describing the total width of the medulla oblongata, show that the overall width ratio of the hindbrain is identical between the two species of *Dromornis* (0.193 vs 0.193, respectively; Table 1B).

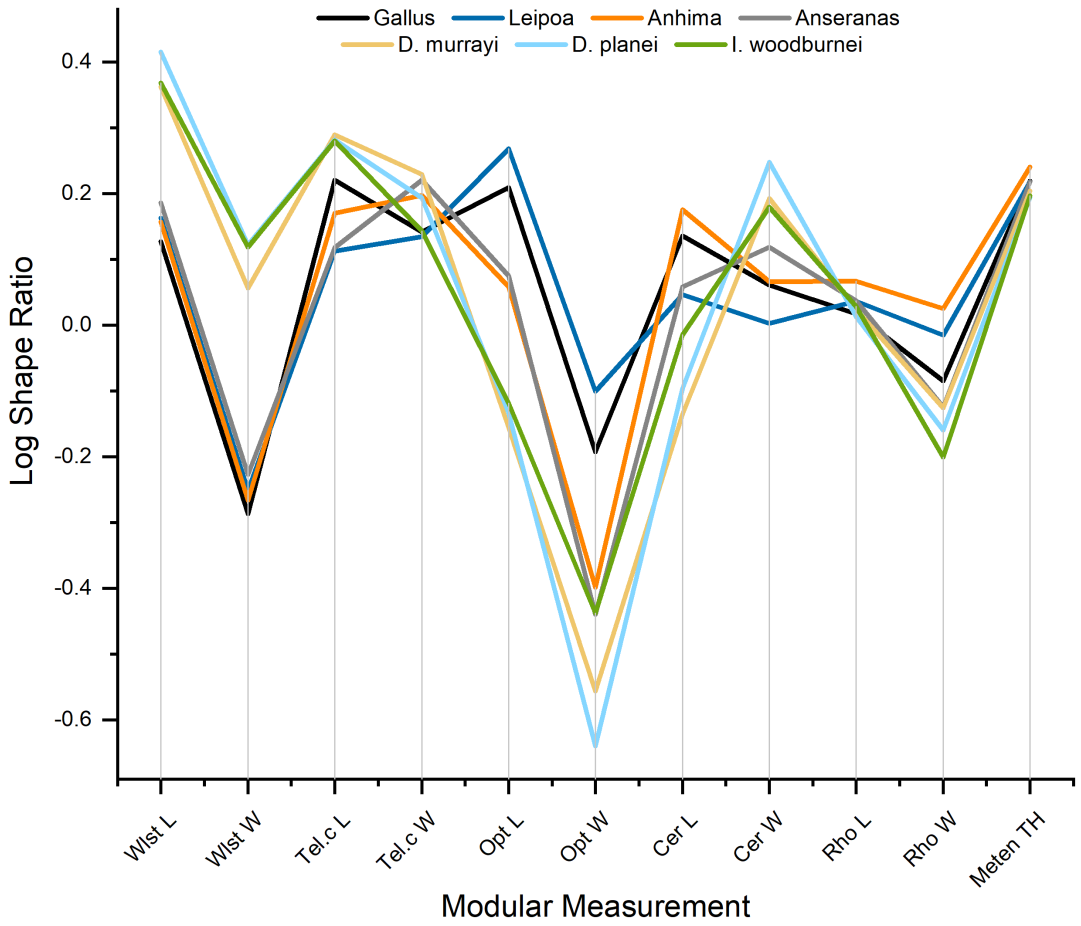

Figure S13. Mean Measurement log shape ratios plot for all galloanseres. Size-standardised log shape ratio data were calculated by the log shape method, where species Measurement values were divided by species endocast volume values and $\log_{10}$ transformed (see Table 1B, **2.6.2**,). **Abbreviations**; **Anhima**; *Anhima cornuta* (SAM B12574); **Anseranas**; *Anseranas semipalmata* (SAM B48035); **Cer L**, cerebellum length; **Cer W**, cerebellum width; **D. murrayi**; *Dromornis murrayi* reconstruction (QM F57984 + QM F57974); **D. planei**; *Dromornis planei* (NTM P9464-106); **Gallus**, *Gallus gallus* (SAM B34041); **I. woodburnei**; *Ilbandornis woodburnei* (QVM:2000:GFV:20); **Leipoa**, *Leipoa ocellata* (SAM B11482); **Meten TH**, metencephalon total height; **Opt L**, optic lobe length; **Opt W**, optic lobe width; **Rho L**, rhombencephalon length; **Rho W**, rhombencephalon width; **Tel.c L**, caudal telencephalon length; **Tel.c W**, caudal telencephalon width; **Wlst L**, wulst length; **Wlst W**, wulst width.

S4.2 *Dromornis* species–*D. planei* compared with *D. stirtoni*

Two specimens of *D. stirtoni* derived from the Alcoota LF were modelled to capture the shape of this, the geologically most recent species of *Dromornis* for which cranial material is available, and compare it to the older forms. Landmarking of the specimens to achieve comparable Modular Slm, Measurement, and Surface Area data used for the older taxa was not possible due to the incomplete nature of the *D. stirtoni* endocast models. However, the overall appearance of the endocasts of *D. stirtoni* are distinctive, in that they appear mediolaterally wider, dorsoventrally compressed rostrally, and somewhat rostrocaudally foreshortened compared with the older dromornithid species. These endocast differences were expected, given the highly derived and

foreshortened nature of crania in the taxon (see Fig. 1), which likely placed structural limits on the housing of the brain.

The cranium of *D. stirtoni*–1 appears to be reasonably well preserved (Figs. S6A–S6H, S7A–S7H). However, the endocranial capsule within suffered taphonomic degeneration of the entire caudodorsal surfaces, directly affecting those areas of the endocast (Figs. S8D–S8E). What is preserved, are primarily the rostroventral endocast surfaces, including a part of the rostrodorsal wulst, the olfactory zone, the rostrolateral eminences of the rostral telencephalon, the mediolateral expansion of the rostroventral caudal telencephalon, and the ventral diencephalon through rhombencephalon structures. The LHS rostrolateral wulst and rostral caudal telencephalon are less well preserved than the RHS. The specimen has experienced a somewhat rostroventrolateral taphonomic 'drift' of cortical bone, that has distorted the LHS of the endocast more so than the RHS (Fig. S8E). The rostroventral eminence of the optic lobe are preserved, but the caudal eminences in the regions of the medial medulla oblongata are less well defined (Fig. S8D). The RHS ramus of the maxillomandibular branch transmitting the maxillary (V_2) and mandibular (V_3) cranial nerves rostroventrolaterally, is relatively well captured, but the LHS is only partially preserved (Fig. S8F). The hypophysis and the ventral rhombencephalon, including the medulla oblongata rostroventrad of the auricula cerebelli, are preserved, but the tubae auditivae are indistinguishable in the CT data. The caudoventral rhombencephalon surface is preserved, approximately to the eminence of the hypoglossal (XII) nerves, which are not present (Fig. S8D). In general, the gross rostroventral morphology in the specimen *D. stirtoni*–1 is discernible, and it has not suffered much overall distortion, but all fine detail has been lost through the taphonomic processes characteristic of the unconsolidated sediments of the Alcoota site (see **2.2** above).

D. stirtoni–2 had suffered the loss of the entire rostral, and much of the rostroventral region of the cranium (Figs. S6I–S6L, S7I–S7P), and consequently preserves only part of the caudodorsal wulst surfaces, of which the RHS is better represented, as the LHS appears to be somewhat rostroventrolaterally distorted (Fig. S8H). The mediolateral eminences of the caudal telencephalon are represented, but the terminal surfaces of these structures, more so on the LHS than the RHS, were not clearly discernible in the CT data with enough consistency to facilitate accurate modelling. *Dromornis stirtoni*–2 preserves the rostrodorsal cerebellum caudally to approximately the eminences of the auricula cerebelli, and also represents the caudoventral rhombencephalon surfaces reasonably well. The endocast is truncated caudoventrally in the region of the eminence of the hypoglossal (XII) nerves, and lacks fine scale detail overall (Figs. S8G–S8H).

Collectively, the endocasts of *D. stirtoni* allow for the appreciation of parts of the rostroventral surfaces (captured by *D. stirtoni*–1, Figs. S8D–S8E), and the caudodorsal surfaces (captured by *D. stirtoni*–2, Figs. S8G–S8H). Thus, an attempt to align these endocast models and compare endocast morphology with that of *D. planei* (Fig. S8A) was made (see **S2.1** above).

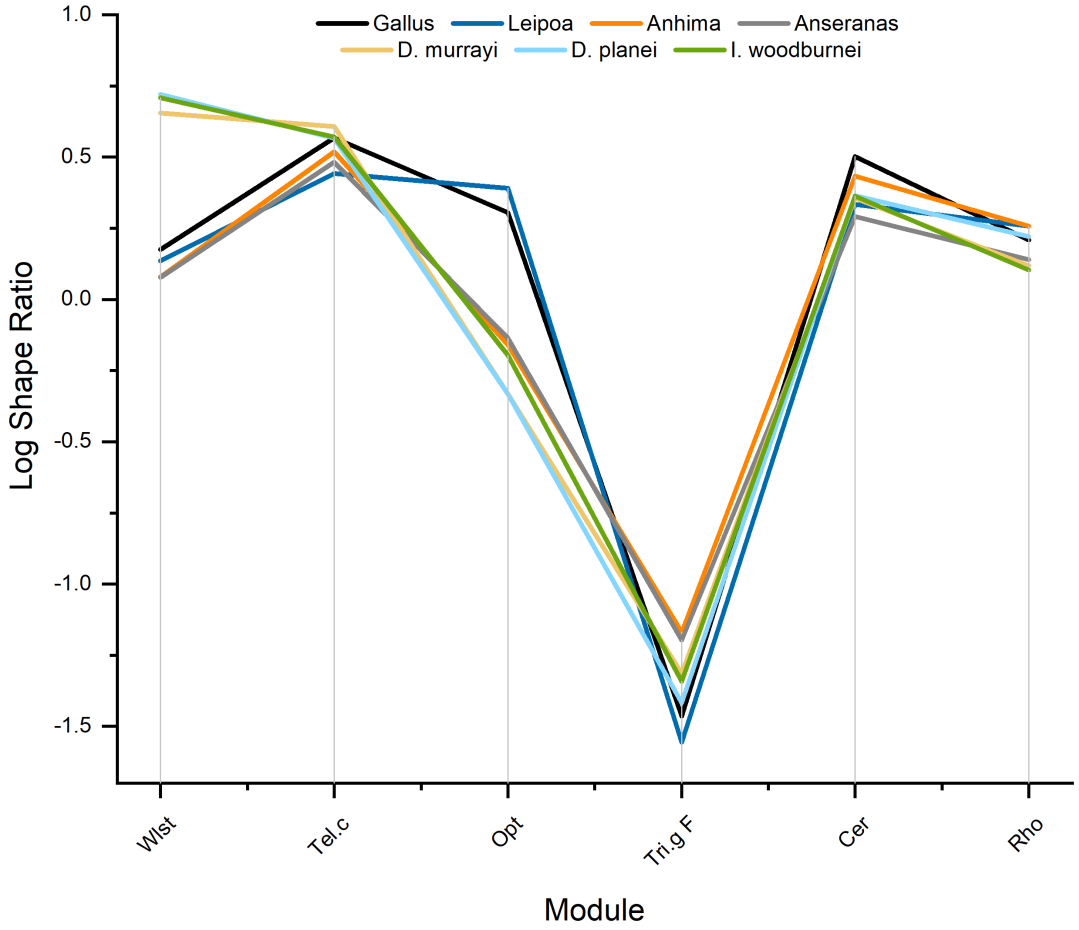

Figure S14. Mean Modular Surface Area ratios plot for all galloanseres. Size-standardised log shape ratio data were calculated by the log shape method, where species modular Surface Area values were divided by species endocast Surface Area values and $\log_{10}$ transformed (see Table 1D, **2.6.2-3**). **Abbreviations**, **Anhima**, *Anhima cornuta* (MV B12574); **Anseranas**; *Anseranas semipalmata* (SAM B48035); **Cer**, cerebellum; **D. murrayi**; *Dromornis murrayi* reconstruction (QM F57984 + QM F 57974); **D. planei**; *Dromornis planei* (NTM P9464-106); **I. woodburnei**; *Ilbandornis woodburnei* (QVM:2000:GFV:20); **Leipoa**, *Leipoa ocellata* (SAM B11482); **Opt**, optic lobe; **Rho**, rhombencephalon; **Tel.c**, caudal telencephalon; **Tri.g F**, trigeminal ganglion face; **Wlst**, wulst.

The *D. planei* model was rescaled larger to have equivalent size to the composite *D. stirtoni* model to facilitate comparison of shape differences. Remaining distortion in the *D. stirtoni* model made alignment of the two endocasts difficult, with necessary rescaling differing by region (8% for lateral RHS and 5% for the rostral region), but overall, the endocast of *D. stirtoni*–1 was approximately 6.5% larger than that of *D. planei*.

S4.2.1 Wulst–in all dromornithid species, the wulst are much hypertrophied structures, unfortunately, these areas are poorly preserved in specimens of *D. stirtoni*. Although an accurate assessment of the true extent of the wulst in *D. stirtoni* was not possible over the whole rostrocaudal endocast surface, several individual CT slices of raw scan data for the *D. stirtoni*–2 specimen preserve elements of the mediolateral wulst profile. For example, Fig. S8L shows a CT slice for *D. stirtoni*–2, where the cortical bone defining the dorsal wulst is caudally displaced from its original position, but

maintains the shape of the dorsal mediolateral curve of the RHS wulst well. The slice also visualises cortical bone elements of the dorsal curve of the LHS wulst, that have displaced into several fragments over time. Another interpretation of these fragments is that they may be a calcite crust lining, formed upon the actual cortical bone of the endocranial capsule during interment (see **2.2**). Either interpretation affords a description of the mediolateral endocranial profile in this area of the skull, showing it to be very similar to that seen in other dromornithid species, for example, the Oligo-Miocene *D. murrayi* (Fig. S8C) and middle Miocene *D. planei* (Fig. S8F). Additionally, the RHS reconstruction of *D. stirtoni* for the lateral profile (Fig. S8J), and the rostral area (Fig. S8K), show the dorsal surfaces of the wulst closely resemble those of *D. planei*. Taken together, these images suggest the wulst in *D. stirtoni* likely had a comparable dorsal profile to other dromornithids (Fig. S8L).

S4.2.2 Caudal telencephalon–*D. stirtoni* displays the characteristic dromornithid state of a clear vallecula transition zone between the dorsal wulst, and the mediolaterally hypertrophied caudal telencephalon (Figs. S8D–S8E). The cerebrum fovea limbica zone (**cfl**, Fig. 3A) preserved in the endocast of *D. stirtoni*–1, agrees with that seen in *D. planei*, and suggests the species share a similar transition into the dorsal caudal telencephalon. The obvious presence of eminences of the rostral telencephalon on the rostroventrolateral surface of the endocast of *D. stirtoni*–1, are indicative of characteristic dromornithid rostroventral endocast morphology too. CT slice images suggest *D. stirtoni* had mediolaterally hypertrophied caudal telencephalon (Fig. S8L), comparable to those seen in *D. murrayi* (Fig. S8C) and *D. planei* (Fig. S8F). Additionally, the brain of *D. stirtoni*, relative to *D. planei*, is more dorsoventrally compressed, represented as an effective reduction in the most ventral eminence of the caudal telencephalon (Figs. S8J–S8K). However, more complete specimens are required to support this observation.

Notably, the caudodorsal compression in *D. stirtoni*, is associated with rostrodorsal rotation of the forebrain endocast surfaces compared with that of *D. planei*, with reference to the positioning of the olfactory zones, and eminences of the rostral telencephalon (Figs. S8J–S8K). The hypophysis and the ramus of the maxillomandibular (V_2+V_3) nerves in the ventral midbrain are well aligned between the specimens in the reconstruction (Fig. S8J), but rostrodorsally from the tractus opticus structure in *D. stirtoni*, all forebrain structures appear rotated around the medial caudal telencephalon into a more dorsally orientated aspect. This rotation is also apparent in the rostral reconstruction (Fig. S8K), where the eminence of the olfactory (I) nerves appear to have shifted dorsally, to approximately the same degree as seen in the RHS lateral reconstruction (Fig. S8J).

S4.2.3 Cerebellum–are comparable only from the RHS lateral aspect between species (Fig. S8J), and show that the dorsal surface of the cerebellum in *D. stirtoni* has a similar rostrocaudal shape to that of *D. planei*, but the dorsal eminence of the cerebellum appears more ventrally orientated. The positioning of the dorsorostrocaudal cerebellum surface appears accurate, as the alignment of the ventral rhombencephalon, reasonably well preserved in both *D. stirtoni* specimens, defined the position of the dorsal cerebellum in the process of reconstruction. Also, the position of the caudal

wulst in *D. stirtoni* agrees with the caudal wulst of *D. planei*, both structures of which are derived from a single specimen (*D. stirtoni*–2). These observations suggest the apparent ventral displacement of the dorsal cerebellum surface in *D. stirtoni*, may reflect a compensatory ventral rotation of the caudodorsal hindbrain, with respect to the rostrodorsal rotation evident in the forebrain (see above).

S4.2.4 Rhombencephalon–this structure in *D. stirtoni* appears to be more ventrally situated than that of *D. planei* (Fig. S8J). Additionally, the distance separating the location of the rhombencephalon in *D. planei*, and those of the two specimens of *D. stirtoni*, more or less equates to the distance the dorsal surfaces of the cerebellum have displaced ventrally, and is similar to the distance the rostroventral zones of the forebrain have rotated dorsally (see above). In effect, the brain of *D. stirtoni* appears rotated about the median plane, whilst the position of the dorsomedial surfaces of the brain have been maintained, effectively foreshortening the overall rostrocaudal length of the endocast in *D. stirtoni* compared with other species of *Dromornis*.

S4.3 Dromornithid species–*D. planei* compared with *I. woodburnei*

Fossils of these dromornithids are derived from the middle Miocene Bullock Creek LF and are presumed similar in age. Comparison of these species enables assessment of morphological differences between the two contemporaneous dromornithid lineages.

S4.3.1 Wulst modules–the 3D modular shape variation plots of the wulst of *D. planei* and *I. woodburnei* (Figs. 5G–5I), show both species share the rostrodorsal hypertrophy of the wulst that largely masks the full extent of the olfactory bulb (Figs. 3A, 3I), compared to its partial visibility in *D. murrayi* (Fig. 3E). Also, the differences in the rostrodorsal wulst apparent between *D. planei* and *I. woodburnei* (Figs. 5G, 5I), are less profound than those between *D. planei* and *D. murrayi* (see **S4.1.1** above; Figs. 5D, 5F). The primary differences between *D. planei* and *I. woodburnei* occur in the rostral regions of the wulst, where those of *D. planei* extend further rostrodorsally (Figs. 5G, 5I). Also, the medial margins of the wulst in *I. woodburnei* track the rostrocaudal fissura interhemispherica zone more closely than in *D. planei* (Figs. 5G–5H). Results for Measurement data show marked differences in overall length (0.415 vs 0.368 respectively; Table 1B), but less so in width (0.122 vs 0.119 respectively; Table 1B) log shape ratios between *D. planei* and *I. woodburnei* (Fig. S12). Results for Surface Area data show that *D. planei* has a somewhat larger log shape ratio than *I. woodburnei* (0.720 vs 0.708, respectively; Fig. S14, Table 1D). Additionally, the dorsolateral margin of the vallecula transition zones, between the caudolateral wulst and the caudodorsal caudal telencephalon in *D. planei,* are located somewhat ventrolaterally in comparison with that of *I. woodburnei* (Fig. 5I), a difference which is more pronounced caudally than rostrally.

S4.3.2 Caudal telencephalon modules–the rostral and rostrodorsal margins of the caudal telencephalon are similar in *D. planei* and *I. woodburnei*, except for the dorsal caudolateral differences in the vallecula zone described above. Modular shape variation plots show the rostrocaudal projection, in the region of the cerebrum pars occipitalis (**coc**, Fig. 3C) of the caudal telencephalon in *D. planei*, appears to be less than that in *I. woodburnei* (Fig. 5I). However, results for

Measurement data show *D. planei* has a very similar overall rostrocaudal length log shape ratio as *I. woodburnei* (0.281 vs 0.280, respectively; Fig. S12, Table 1B). Notably, *D. planei* has a greater log shape ratio for caudal telencephalon total width than *I. woodburnei* (0.447 vs 0.418, Table 1B). The ventral margins of the caudal telencephalon are distinctive in *D. planei*, having a noticeably more pronounced ventral eminence in the region of the fissura subhemispherica (**fs**, Fig. 3B) than *I. woodburnei* (Fig. 5I). Results for Measurement data show *D. planei* has a much greater dorsoventral width log shape ratio than *I. woodburnei* (0.193 vs 0.143, respectively; Fig. S12, Table 1B). In fact, the dorsoventral width log shape ratio of the caudal telencephalon in *I. woodburnei* is less than those of both species of *Dromornis* (see **S4.4.2** below). Results for Surface Area data show that log shape ratios between the *D. planei* and *I. woodburnei* are somewhat similar (0.566 vs 0.571, respectively; Fig. S14, Table 1D).

S4.3.3 Cerebellum module–the rostral cerebellum of *D. planei* and *I. woodburnei* are of similar rostrodorsoventral height (Fig. 5I). Also, the mediolateral margins are similar, and suggest all dromornithids may have comparable cerebellum shape mediolaterally (Figs. 5H–5I). However, a distinct difference between species, is that the rostrocaudal surface of the cerebellum in *I. woodburnei* projects further caudodorsally (Figs. 5H–5I), prior to turning ventrally to grade into the dorsal medulla spinalis caudally at the foramen magnum. Results for Measurement data describe these characteristics well, where rostrocaudal length log shape ratios are smaller for *D. planei* than for *I. woodburnei* (-0.096 vs 0.015 respectively; Fig. S12, Table 1B), but width log shape ratios are larger for *D. planei* (0.248 vs 0.180, respectively; Fig. S12, Table 1B). Results for Surface Area data show that log shape ratios for *D. planei* are only somewhat larger than that of *I. woodburnei* (0.365 vs 0.363, respectively; Fig S14, Table 1D). Additionally, the rostral dorsomediolateral border of the cerebellum of *I. woodburnei*, is somewhat rostrocaudally curved as compared to that of *D. planei*, which describes a straighter dorsomediolateral margin rostrally (Fig. 5H).

S4.3.4 Rhombencephalon module–the mediolateral profile of the rhombencephalon in *I. woodburnei* is noticeably more dorsoventrally curved than that of *D. planei*, which is rostrocaudally and mediolaterally less ventrally pronounced (Fig. 5I). Results for Measurement data show rostrocaudal length log shape ratios are somewhat smaller for *D. planei* than for *I. woodburnei* (0.013 vs 0.029, respectively; Fig. S12, Table 1B), but mediolateral width log shape ratios are markedly larger (-0.159 vs -0.201, respectively; Fig. S12, Table 1B), so this module is relatively longer and narrower in *Ilbandornis*. Furthermore, the more ventral location of the rhombencephalon in *I. woodburnei*, and the position of the rhombencephalon relative to the most dorsal eminence of the cerebellum, is described well by the total height log shape ratio of the metencephalon (cerebellum + pons, see Fig. 2C, **2.6.2**), which is only slightly greater in *D. planei* than in *I. woodburnei* (0.194 vs 0.197 respectively; Fig. S12, Table 1B). When endocast size is accounted for, the height of the hindbrain is somewhat similar between *D. planei* and *I. woodburnei*. Notably, the Measurement width log shape ratio of the medulla oblongata, describing the mediolateral width of the hindbrain, is much

larger in *D. planei* (0.193 vs 0.119 respectively; Table 1B). The slightly greater rostrocaudal length log shape ratio (see above) of the rhombencephalon in *I. woodburnei*, is likely due to the deeper ventromediolateral rhombencephalon profile in the species (Fig. 5I). Results for Surface Area data show that *D. planei* has a markedly larger log shape ratio than *I. woodburnei* (0.221 vs 0.103, respectively; Fig. S14, Table 1D)

S4.4 Dromornithid species–*D. murrayi* compared with *I. woodburnei*

In this section, we compare the late Oligocene species of *Dromornis* with the younger, middle Miocene *Ilbandornis* lineage, to assess any distinctions between the two lineages that may reveal correlations with those identified between the middle Miocene *Dromornis* and *Ilbandornis* lineages.

S4.4.1 Wulst modules–of *I. woodburnei* extend further rostrodorsally, caudodorsally and mediolaterally than those of *D. murrayi* (Figs. 5J, 5K). Results for Measurement data show *D. murrayi* has only a somewhat smaller log shape ratio for length (0.362 vs 0.368 respectively; Table 1B), but the width log shape ratio (0.056 vs 0.119 respectively; Fig. S12, Table 1B) is much larger in *I. woodburnei*. Results for Surface Area show that *D. murrayi* has a notably smaller log shape ratio that *I. woodburnei* (0.655 vs 0.708, respectively; Fig. S14, Table 1D). Additionally, the medial margins of the wulst in *I. woodburnei* track the rostrocaudal fissura interhemispherica zone more closely than in species of *Dromornis* (see Figs. 5H–5K, **S4.3.1**). The mediolateral hypertrophy of wulst of *I. woodburnei* results in the vallecula transition zone being slightly displaced ventrolaterally, between the dorsal caudolateral wulst and the dorsal caudal telencephalon compared to *D. murrayi* (Figs. 5J, 5K–5L). These shifts in the vallecula transition zones in *I. woodburnei*, occurred primarily in caudolateral areas of the caudal wulst. Overall, the wulst of *D. murrayi* are more gracile than those of *I. woodburnei* (Figs. 5J–5L).

S4.4.2 Caudal telencephalon module–contrary to what was observed between *D. planei* and *D. murrayi*, the relatively larger overall length and width log shape ratios for wulst in *I. woodburnei*, was not accompanied by a compensatory ventral rotation of the dorsolateral surface of the caudal telencephalon, so that the dorsolateral vallecula margins of the caudal telencephalon in *D. murrayi* are only marginally distinct from those of *I. woodburnei* (Figs. 5K–5L; see also above). The rostral and rostrodorsal margins of the caudal telencephalon are comparable between specimens, but the caudal margins are distinct in that those of *I. woodburnei* project further caudally in the region of the cerebrum pars occipitalis, than in *D. murrayi* (Fig. 5L). Results for Measurement data, however, show *D. murrayi* has a somewhat larger rostrocaudal length log shape ratio than *I. woodburnei* (0.289 vs 0.280 respectively; Fig. S12, Table 1B). This is likely due to the greater lateral eminence of the caudal telencephalon in *D. murrayi*, described well by caudal telencephalon total width log shape ratios showing that of *D. murrayi* is larger than that of *I. woodburnei* (0.443 vs 0.418, respectively; Table 1B). The methods used to compute Measurement values captured the rostrocaudal curve of the lateral eminence of the caudal telencephalon (see Fig. 2F). Consequently, rostrocaudal length log shape ratios also reflect the greater lateral projection of the caudal telencephalon in *D. murrayi*, likely

offsetting distinctions of the caudal telencephalon between species apparent in the shape variation plots. Therefore, rostrocaudal length log shape ratios likely do not reflect the clear shape distinction of the caudal telencephalon between species particularly well. Shape variation plots show the most ventral eminences of the caudal telencephalon, in the region of the fissura subhemispherica, are noticeably more pronounced in *D. murrayi* than in *I. woodburnei* (Fig. 5L). These observations are supported by results for Measurement data showing *D. murrayi* has larger dorsoventral width log shape ratios than *I. woodburnei* (0.229 vs 0.143, respectively; Fig. S12, Table 1B). Results for Surface Area data show that the oldest species of *Dromornis* has a larger log shape ratio than *I. woodburnei* (0.608 vs 0.571, respectively; Fig. S14, Table 1D). The differences between *D. murrayi* and *I. woodburnei* in the dorsal caudal telencephalon, is comparable with those observed in the dorsal caudal telencephalon in *D. planei*, but to a lesser degree (Figs. 5D, 5E–5F).

S4.4.3 Cerebellum module–the rostrodorsal eminence of the cerebellum in *I. woodburnei*, with respect to the mediolateral margins, projects further dorsally than in *D. murrayi* (Fig. 5L). The rostrodorsal cerebellum of *D. murrayi* has a flatter dorsomediolateral margin than that of *I. woodburnei*, which displays a more rostrally projecting mediolateral curve (Fig. 5K). Additionally, the caudodorsal margins in *D. murrayi* are mediolaterally flatter, and do not project as far caudally as in *I. woodburnei* (Figs. 5K–5L). These characteristics are reflected by results for Measurement data, showing *D. murrayi* has a smaller overall rostrocaudal length log shape ratio than *I. woodburnei* (-0.135 vs 0.015, respectively; Fig. S12, Table 1B). From the dorsal aspect, the dorsomediolateral profile of the cerebellum between species is quite similar (Fig. 5K), with the caudal width of the cerebellum appearing marginally wider in *D. murrayi*. These observations are supported by results showing *D. murrayi* has a larger width log shape ratio than *I. woodburnei* (0.193 vs 0.180, respectively; Fig. S12, Table 1B). Results for Surface Area data show that *D. murrayi* had a somewhat smaller log shape ratio than *I. woodburnei* (0.355 vs 0.363, respectively; Fig. S14, Table 1D). The overall lateral profile of the cerebellum between these species, show that *I. woodburnei* displays a steeper rostrocaudal caudal profile, beginning at the medial dorsal cerebellum. This is likely due to the rostrodorsal through dorsomedial cerebellum hypertrophy in *I. woodburnei* (Figs. 5K–5L).

S4.4.4 Rhombencephalon module–the rostral margin of the rhombencephalon in *I. woodburnei*, describes a more rostrally projecting mediolateral curve (Fig. 5L), than those of both species of *Dromornis*, which show flatter rostromediolateral margins (Figs. 5F, 5I). The ventral position of the rhombencephalon surface in *D. murrayi* is similar to that of *I. woodburnei* in shape space (Fig. 5L). The mediolateral profile in the *D. murrayi* and *I. woodburnei* rhombencephalon are more ventrally curved than that of *D. planei*, which displays a flatter mediolateral shape (Figs. 5F, 5I; and above). Results for Measurement data show the rostrocaudal length log shape ratio of *D. murrayi* is very similar to *I. woodburnei* (0.024 vs 0.029, respectively; Fig. S12, Table 1B), but the mediolateral width log shape ratio of *D. murrayi* is markedly greater (-0.125 vs -0.201; Fig. S12,

Table 1B). These trends are similar to those noted in the comparisons of *D. planei* and *I. woodburnei* (see **S3.3.4** above). Additionally, the total width log shape ratio for the medulla oblongata, shows that *D. murrayi* has a notably wider hindbrain than *I. woodburnei* (0.193 vs 0.119 respectively; Table 1B). The log shape ratio measuring the overall height of the metencephalon (cerebellum + pons), shows that *D. murrayi* has a somewhat taller overall hindbrain height than *I. woodburnei* (0.204 vs 0.197, respectively; Fig. S12, Table 1B). Results for Surface Area data show that *D. murrayi* had a larger log shape ratio than *I. woodburnei* (0.119 vs 0.103, respectively; Fig. S14, Table 1D).

S5 Dromornithid specimens compared with the extant Galloanseres

In this section, we compare the dromornithid condition with those of the extant galloanseres. Morphological distinctions between specimens are ascertained with reference to Measurement log shape ratio results (see Fig. S13, Table 1B), Surface Area log shape ratio results (Fig. S14, Table 1D), and the endocast models of *Gallus gallus* (SAM B34041; Figs. 4E–4H), *Leipoa ocellata* (SAM B11482; Figs. 4I–4L), *Anhima cornuta* (MV B12574; Figs. 4A–4D), *Anseranas semipalmata* (SAM B48035; Figs. 4M–4P), *Dromornis planei* (NTM P9464-106; Figs. 3A–3D), *D. murrayi* reconstruction (QM F57984 + QM F57974, Figs. 3E–3H), and *Ilbandornis woodburnei* (QVM:2000:GFV:20; Figs. 3I–3L).

S5.1 Innervation–the olfactory bulb of *A. semipalmata* displays hypertrophy in excess of that seen in *A. cornuta*, which is somewhat more than that of *L. ocellata* and *G. gallus* (Figs. 4M, 4A, 4I, 4E). The olfactory zones of these galloanseres appear to be wholly external to the rostral telencephalon, as the olfactory bulbs, more distinct in *A. semipalmata* and *A. cornuta*, but less so in *L. ocellata* and *G. gallus*, appear to be slightly constricted immediately rostrad of the rostral telencephalon. This condition is distinct to that observed in dromornithids (e.g. Figs. 3A, 3E, 3I). The morphologies of the trigeminal ganglia are similar between species, in that the ophthalmic (V_1) branch is widely separated from the maxillomandibular (V_2+V_3) branch, and all display a ganglionic bridge between the two nerve branches. However, the dromornithid maxillomandibular (V_2+V_3) branch displays a potentially synapomorphic morphology where it passes through the cranium. For example, the canalis n. maxillomandibularis passes minimally 20 mm caudoventrolaterally (in *Dromornis*), after entering the skull at the foramen n. maxillomandibularis (**fmx**, Figs. S4K–S4L, S5K; **V_2+V_3**, S5L) in all dromornithids assessed. In the other species, excluding *G. gallus*, this distance is markedly shorter, and the nerves exit the skull almost directly after separation from the ventral surface of the optic lobe (Figs. 4I–4J, 4L, 4A–4B, 4D, 4M–4N, 4P). In the phasianid *G. gallus* however (see Figs. 4E–4F, 4H), there occurs transmission of the maxillomandibular (V_2+V_3) nerves through the cranium that, although somewhat shorter than that observed in dromornithids, is longer than observed in the other galloanseres (see also **4.1.2**).

Results for Measurement data show that when endocast size is accounted for, trigeminal ganglion length log shape ratios for *D. murrayi*, *D. planei* and *I. woodburnei* (-0.256, -0.276, -0.252,

respectively; Table 1B) are actually shorter than that of *L. ocellata* (-0.358, Table 1B), but somewhat longer than those of *G. gallus* and *A. cornuta* (-0.194, -0.167, respectively; Table 1B). *Anseranas semipalmata* (-0.143, Table 1B) has the shortest trigeminal ganglion length log shape ratio of all species. Log shape ratios for trigeminal ganglion width show that the dromornithids *D. murrayi*, *D. planei* and *I. woodburnei* (-0.405, -0.452, -0.379, respectively; Table 1B) have wider trigeminal ganglion morphology than *G. gallus* (-0.285, Table 1B). However, *L. ocellata* (-0.418, Table 1B) has a wider trigeminal ganglion than *D. murrayi*, and *I. woodburnei*, but not *D. planei.* The trigeminal ganglion of *A. cornuta* (-0.587, Table 1B) is wider than that of all dromornithids, and *A. semipalmata* (-0.604, Table 1B) has the widest trigeminal ganglion of all specimens. Results for Surface Area data show that the galliforms *L. ocellata* and *G. gallus* (-1.556, -1.464, respectively; Fig. S14, Table 1D) have the smallest Surface Area log shape ratios for the truncated face of the maxillomandibular (V_2+V_3) branch of the trigeminal (V) nerve complex, followed by the dromornithids *D. planei*, *I. woodburnei*, and *D. murrayi* (-1.418, -1.342, -1.314 respectively; Fig. 14, Table 1D). The anseriforms *A. semipalmata* and *A. cornuta* (-1.197, -1.169, respectively, Fig. 14, Table 1D) have the largest maxillomandibular (V_2+V_3) surface areas for all galloanseres assessed.

In dromornithids, the glossopharyngeal (IX) and vagus (X) nerves separate somewhat caudoventrolaterally from the eminence of the proximal ganglion from the rhombencephalon surface (Figs. 3A, 3D–3E, 3H–3I, 3L). This condition is similar to that seen in *G. gallus* (Figs. 4E, 4H) and *A. semipalmata* (Figs. 4M, 4P), but separation occurs somewhat further distally in dromornithids. The condition is, to a lesser extent, similar to that seen in *A. cornuta* (Figs. 4A, 4D), but distinct to that of *L. ocellata* (Figs. 4I, 4L). The eminence of the hypoglossal (XII) nerves which typically comprise a rostral (XIIr) and caudal (XIIc) branch (e.g. Fig. 4D), is represented by one nerve root at either side of the caudoventrolateral medulla oblongata in dromornithids (Fig. 3D), so differing from the condition in the extant galloanseres (Figs. 4D, 4H, 4L, 4P).

S5.2 Wulst modules–these structures in dromornithids differ from any seen in the extant galloanseres (**wlst**, Figs. 3B–3D, 4C). Measurement data results show length log shape ratios for *G. gallus*, *L. ocellata*, *A. cornuta*, and *A. semipalmata* (0.127, 0.163, 0.157, 0.186, respectively; Fig. S13, Table 1B), and width log shape ratios (-0.287, -0.251, -0.266, -0.227; respectively; Fig. S13, Table 1B) are substantially smaller, than the length (0.362, 0.415, 0.368, respectively; Fig. S13, Table 1B) and width (0.056, 0.122, 0.119, respectively; Fig. S13, Table 1B) log shape ratios for *D. murrayi*, *D. planei* and *I. woodburnei*. Results for Surface Area data show that log shape ratios for the dromornithids *D. murrayi*, *D. planei* and *I. woodburnei* (0.655, 0.720, 0.708, respectively; Fig. S14, Table 1D) are substantially larger than those of the galloanseres *G. gallus*, *L. ocellata*, *A. cornuta*, and *A. semipalmata* (0.176, 0.136, 0.079, 0.078, respectively; Fig. S14, Table 1D). These results show that when endocast absolute size is accounted for, *G. gallus* and *L. ocellata* have the largest wulst surface areas among the extant galloanseres, and the anseriforms A. cornuta and *A. semipalmata* the smallest, respectively.

S5.3 Rostral telencephalon modules–evidence of the rostral telencephalon is conspicuously absent on the external morphology of dromornithid endocasts, and only present rostrally as twin eminences ventromediolaterad of the olfactory bulb, on either side of the rostromedial surface of the endocast (**tel.r**, Figs. 3B, 3D). Consequently, detailed comparisons are not possible between the rostral telencephalon of dromornithids and those of the other galloanseres, and we present results for the extant species only.

Results for Measurement data show *A. semipalmata* has the largest length log shape ratio (0.123, Table 1B), followed by *L. ocellata* and *A. cornuta* (-0.011, -0.052, respectively; Table 1B). *Gallus gallus* has the shortest rostral telencephalon length log shape ratio (-0.221, Table 1B) of all species. Width log shape ratios show that *A. semipalmata* (-0.049, Table 1B) has a wider rostral telencephalon than *A. cornuta* (-0.158, Table 1B), followed by *L. ocellata* (-0.257, Table 1B). *Gallus g**allus* (-0.365, Table 1B), has the narrowest rostral telencephalon log shape ratio of all extant galloanseres. Results for Surface Area data show *G. gallus* has the smallest rostral telencephalon surface area (-0.299; Table 1D), followed by *L. ocellata* and *A. cornuta* (-0.006, 0.039, respectively; Table 1D). *A. semipalmata* has the largest surface area of the extant galloanseres (0.343; Table 1D).

S5.4 Caudal telencephalon modules–results for Measurement data show the dromornithids *D. murrayi*, *D. planei* and *I. woodburnei* have larger rostrocaudal length log shape ratios than all other specimens (0.289, 0.281, 0.280, respectively; Fig. S13, Table 1B). The length log shape ratio for *G. gallus* (0.220, Fig. S13, Table 1B), is most similar to those of the dromornithids, followed by that of *A. cornuta* (0.170, Fig. S13, Table 1B). *A. semipalmata* and *L. ocellata* (0.118, 0.113, respectively; Fig. S13, Table 1B) have somewhat similar length log shape ratios, with that of *L. ocellata* being the smallest of the galloanseres. Dorsoventral width log shape ratios show *A. semipalmata* and *A. cornuta* (0.220, 0.198, respectively; Fig. S13, Table 1B) have a dorsoventrally wider caudal telencephalon than *D. planei*, *G. gallus*, *I. woodburnei,* and *L. ocellata* (0.193, 0.142, 0.143, 0.134, respectively; Fig. S13, Table 1B). The dromornithid *D. murrayi* has the largest caudal telencephalon dorsoventral width log shape ratio (0.229, Fig. S13, Table 1B), and *L. ocellata* the smallest for the galloanseres. Measurement log shape ratios describing the total caudal endocast width, show the dromornithids *D. murrayi*, *D. planei* and *I. woodburnei* (0.443, 0.447, 0.418, respectively; Table 1B) have the largest endocast total width of the galloanseres. Of the extant galloanseres, the anseriforms *A. cornuta* and *A. semipalmata* (0.382, 0.368, respectively; Table 1B) have the widest endocast total width, followed by the galliforms *G. gallus*, and *L. ocellata* (0.355, 0.354, respectively; Table 1B). The megapodiid *L. ocellata* has the smallest endocast width of the galloanseres. Results for Surface Area data show the dromornithid *D. murrayi* (0.608; Fig. S14, Table 1D) has the largest surface area of all specimens, followed by *I. woodburnei* and *D. planei* (0.571, 0.566; Fig. S14, Table 1D). The megapodiid *L. ocellata* (0.443; Fig. S14, Table 1D) has the smallest log shape ratio, followed by *A. semipalmata* and *A. cornuta* (0.482, 0.519, respectively; Fig. S14, Table 1D). The phasianid *G. gallus* (0.569; Fig. S14, Table 1D) has the largest surface area log shape ratio for the extant galloanseres.

S5.5 Optic lobe modules–in dromornithids, optic lobe structures appear somewhat hypotrophied, and are not as well defined as in the other galloanseres (e.g. Figs. 3–4). The megapodiid *L. ocellata* displays the most hypertrophied state (Figs. 4I–4J, 4L), followed by *G. gallus* (Figs. 4E–4F, 4H), and *A. semipalmata* (Figs. 4M–4N, 4P). The optic lobe of *A. cornuta* appears to be the most hypotrophied (Figs. 4A–4B, 4D) among the extant specimens. Results for Measurement data show *L. ocellata* has the largest length log shape ratio for all specimens (0.268; Fig. S13, Table 1B), followed by *G. gallus* (0.210, Fig. S13, Table 1B). The anseriforms *A. semipalmata* and *A. cornuta* (0.075, 0.058, respectively; Fig. S13, Table 1B), have similar length log shape ratios. The extant galloanseres all have markedly larger optic lobe length log shape ratios than the dromornithids *D. murrayi*, *D. planei* and *I. woodburnei* (-0.156, -0.134, -0.119, respectively; Fig. S13, Table 1B), with *I. woodburnei* showing the largest log shape ratio of the dromornithids. Similarly, the optic lobe width log shape ratio for *L. ocellata* is the largest (-0.101; Fig. S13, Table 1B), followed by *G. gallus* and *A. cornuta* (-0.193, -0.398, respectively; Table 1B). *I. woodburnei* and *A. semipalmata* have very similar width log shape ratios (-0.438, -0.440, respectively; Fig. S13, Table 1B), followed by the dromornithids *D. murrayi* and *D. planei* (-0.556, -0.640, respectively; Fig. S13, Table 1B). Results for Surface Area data show that *Dromornis* species *D. murrayi* and *D. planei* have the smallest, and identical log shape ratios (-0.332, -0.332, respectively; Fig. S14, Table 1D), followed by *I. woodburnei* (-0.196: Fig. S14, Table 1D). Surface area log shape ratios for the anseriforms *A. cornuta* and *A. semipalmata* (-0.159, -0.137, respectively; Fig. S14, Table 1D) are quite similar to those of the dromornithids, and the galliforms *G. gallus* and *L. ocellata* (0.306, 0.391, respectively; Fig. S14, Table 1D) have the largest surface area log shape ratios of all specimens.

S5.6 Cerebellum module–those of dromornithids are characteristically rostrocaudally compressed and mediolaterally expanded (see **3.2.6**). From the lateral aspect, the dromornithid cerebellum forms a rostrocaudal shelf rostrally, and turns sharply ventrally in the vicinity of the dorsolateral auricula cerebelli, to meet the caudodorsal medulla spinalis at the foramen magnum. This condition is similar to that seen in *G. gallus*, *L. ocellata*, and in *A. semipalmata*, with the anseranatid showing a larger and more pronounced ventral transition (Figs. 4E, 4I, 4M). However, this characteristic is not evident in the caudodorsal cerebellum of the anhimid *A. cornuta*, which displays a comparably gradual caudoventral transitional gradient (Fig. 4A). In dorsal aspect, rostrad of the foramen magnum, all extant galloanseres display progressive rostrolateral divergence of lateral cerebellum margins, prior to grading into the cerebrum pars occipitalis regions of the caudal telencephalon (Figs. 4C, 4G, 4K, 4O). This condition is not evident in dromornithids which display a more abrupt dorsomediolateral divergence of cerebellum margins, after the rostral transmission of the medulla spinalis through the foramen magnum. Thereafter, the dorsolateral cerebellum margins describe a somewhat parallel rostrocaudal transition into the cerebrum pars occipitalis regions (Figs. 3C, 3G, 3K). Results for Measurement data show cerebellum length log shape ratios for *D. murrayi*, *D. planei* and *I. woodburnei* (-0.135, -0.096, -0.015, respectively; Fig. S13, Table 1B) are much

rostrocaudally shorter than *G. gallus*, *L. ocellata*, *A. cornuta*, and *A. semipalmata* (0.136, 0.046, 0.176, 0.058, respectively; Fig. S13, Table 1B). Conversely, the mediolateral cerebellum width log shape ratios for *D. murrayi*, *D. planei* and *I. woodburnei* (0.193, 0.248, 0.180, respectively; Fig. S13, Table 1B) are all greater than those of *G. gallus*, *L. ocellata*, *A. cornuta* and *A. semipalmata* (0.061, 0.003, 0.067, 0.119, respectively; Fig. S13, Table 1B), with that of *A. semipalmata* most approaching those of the dromornithids. Results for Surface Area data show that, of the dromornithids, *D. planei* (0.365; Fig. S14, Table 1D) has the largest log shape ratio, followed by *I. woodburnei* and *D. murray*i (0.363, 0.355, respectively; Fig. S14, Table 1D). Results for the extant galloanseres show *A. semipalmata* (0.292; Fig. S14, Table 1D) has the smallest log shape ratio for all specimens. *Leipoa ocellata* (0.334; Fig. S14, Table 1D) approaches those of the dromornithids, and is most similar to that of *I. woodburnei*. *Anhima cornuta* (0.434; Fig. S14, Table 1D) has a larger log shape ratio than all dromornithids, and the *G. gallus* (0.502; Fig. S14, Table 1D) has the largest log shape ratio of all galloanseres.

S5.7 Rhombencephalon module–the rhombencephalon between species are distinct, with the dromornithids having somewhat flat ventral surfaces rostrocaudally and mediolaterally, and the extant galloanseres display much ventrally hypertrophied surfaces in comparison (**rho**; Figs. 4A, 4B, 4D). Results for Measurement data show length log shape ratios for *D. murrayi*, *D. planei* and *I. woodburnei* (0.024, 0.013, 0.029, respectively; Fig. S13, Table 1B) are similar to *G. gallus*, *L. ocellata* and *A. semipalmata* (0.017, 0.037, 0. 037, respectively; Fig. S13, Table 1B), but that of *A. cornuta* is the largest for all specimens (0.067; Fig. S13, Table 1B). Rhombencephalon width log shape ratios for *G. gallus*, *L. ocellata* and *A. cornuta* (-0.085, -0.015, 0.025, respectively; Fig. S13, Table 1B) are all greater than those of *D. murrayi*, *D. planei* and *I. woodburnei* (-0.125, -0.159, -0.201, respectively; Fig. S13, Table 1B). The width log shape ratio of *A. semipalmata* is very similar to that of *D. murrayi* (-0.124; Fig. S13, Table 1B), and that of *A. cornuta* is the largest of all species. Results for Measurement data describing the width of the medulla oblongata, show the dromornithids *D. murrayi*, *D. planei* (0.193, 0.193, respectively; Table 1B) have greater ventral hindbrain width log shape ratios than *G. gallus*, *L. ocellata*, *A. cornuta* and *A. semipalmata* (0.143, 0.074, 0.088, 0.065, respectively; Table 1B).

Interestingly, the hindbrain width log shape ratio for *I. woodburnei* (0.119; Table 1B) is less than that of *G. gallus*, and only somewhat larger than those of *A. cornuta*, *L. ocellata* and *A. semipalmata* (Table 1B, and above). However, the log shape ratio describing the total height of the hindbrain in *D. murrayi*, *D. planei* and *I. woodburnei* (0.204, 0.194, 0.197, respectively; Table 1B), show the depth, or ventral projection of the rhombencephalon in *G. gallus*, *L. ocellata, A. cornuta*, and *A. semipalmata* (0.219, 0.218, 0.240, 0.218, respectively; Table 1B) is greater than in the dromornithids. Results for Surface Area data show that the dromornithids *I. woodburnei* and *D. murrayi* (0.103, 0.119, respectively; Fig. S14, Table 1D) have the smallest log shape ratios, followed by *A. semipalmata* and *G. gallus* (0.140, 0.210, respectively; Fig. S14, Table 1D). The dromornithid

D. planei (0.221; Fig. S14, Table 1D) has a somewhat similar log shape ratio as *G. gallus*, and *A. cornuta* and *L. ocellata* (0.258, 0.258, respectively; Fig. S14, Table 1D), show the largest log shape ratios among all galloanseres.

S6 Gastrolith data

S6.1 Estimated body mass data–were computed for: Holocene New Zealand (NZ) palaeognath moa, *Dinornis robustus* (Owen, 1846), n = 5; *Euryapteryx curtus gravis* (Owen, 1870), n = 1; Australian emu (*Dromaius novaehollandiae*; n = 1), and dromornithid (*Genyornis newtoni*; n = 2) taxa (full specimen details are presented in Table S1A), for which complete gizzard data are associated (see below). Body masses were calculated using Alexander's [179] algorithm for femur length (Fem L), ensuring estimated mass comparability across specimens, as tibiotarsi circumference metrics were unavailable for the moa. However, the fossil specimen of *G. newtoni* (uncatalogued, field code CB 2018-23), lacked complete femora, therefore the mass estimation for CB 2018-23 was taken as the mean mass estimation for *G. newtoni* 'unsexed data' (n = 22), from Grellet-Tinner *et al*. [32] (table A2), which were computed using Campbell & Marcus' [180] tibiotarsus least-shaft circumference algorithm. This value falls within the estimated mass range for *G. newtoni* (SAM P.53833, Table S1) using Alexander's [179] algorithm.

S6.2 Gizzard data–were compiled from the literature [19 (table 5.11), Worthy Unpubl. Data] and by directly measuring the complete mass and gastrolith sizes of associated gizzard contents for those fossil and extant specimens, for which body mass data were estimated (see above). Gastrolith size is the narrowest width of the two largest dimensions for each gastrolith measured [*sensu* 113]. Estimated body mass, gizzard mass and gastrolith size results are presented in text and in Table S1A. Size-standardised gizzard mass and gastrolith ratios were calculated by dividing $\log_{10}$ transformed gizzard mass and gastrolith size values by $\log_{10}$ transformed specimen mean body mass values (see Table S1B).

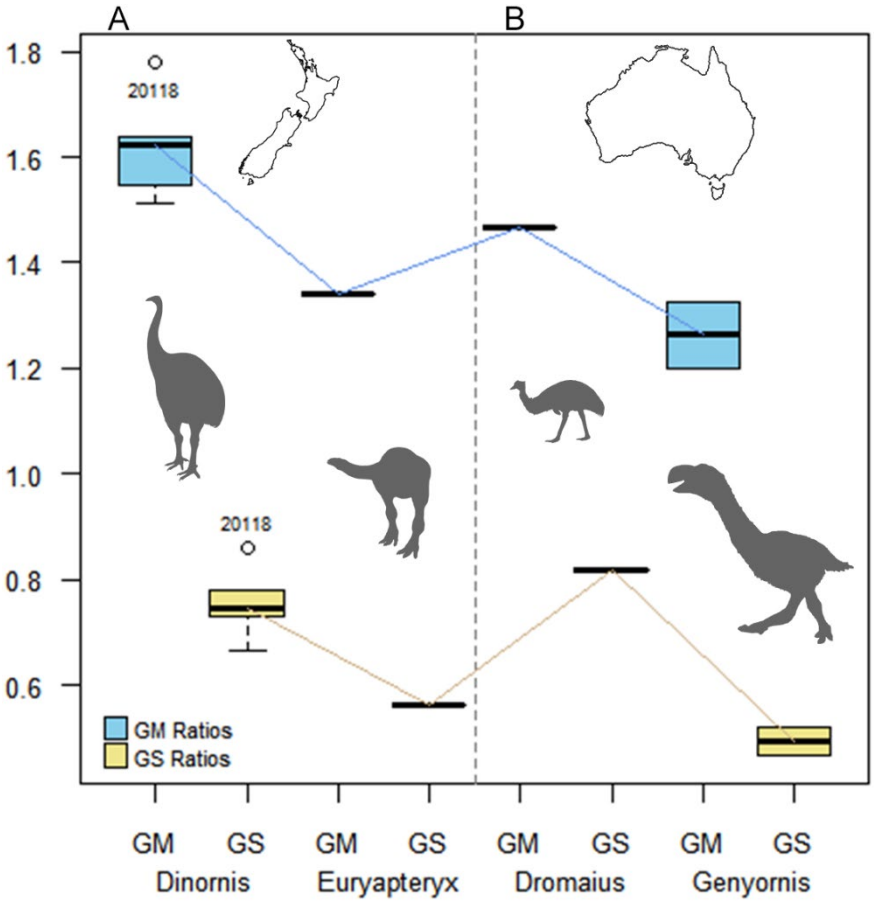

Figure S15. Quantile boxplots of gizzard mass (GM) and gastrolith size (GS) ratios, with respect to mean body mass (BM), for: **A**, New Zealand palaeognath moa (*Dinornis robustus*, n = 5; *Euryapteryx curtus gravis*, n = 1); and **B**, Australian palaeognath emu (*Dromaius novaehollandiae*, n = 1); and dromornithid (*Genyornis newtoni*, n = 2) specimens, for which complete gizzard data are associated (see Tables S1A–S1B, **S6.2**). Boxplot medians are linked to visualise distinctions between the two groups of data. Upper and lower bounds of each boxplot represent the upper and lower quartiles respectively, the horizontal line represents the median, and whiskers represent standard deviation at 1.5 IQR. *D. robustus* GM and GS ratios boxplot outliers (open circles) represent the PV specimen which falls outside 1.5 IQR. Full details for all specimens are given in Table S1A. See **S1** for outline maps and silhouette credits. **Abbreviations**. **BM**, mean body mass; **GM**, gizzard mass; **GS**, gastrolith size; **IQR**, inter-quartile range (25–75%); **PV**, Pyramid Valley Swamp.

S6.3 Results for estimated body mass, gizzard mass and gastrolith size ratios

Results for body mass data, show that *Genyornis newtoni* has the largest mean body mass for the species for which gizzard stone datasets were analysed, followed by *Dinornis robustus*, *Euryapteryx curtus gravis,* and *Dromaius novaehollandiae* (mean body mass (kg) = 204.2, 135.8, 121.9, 42.1, respectively; Table S1A). The largest gizzard mass ratio, with respect to mean body mass, is that of *D. robustus*, followed by those of *D. novaehollandiae, E. c. gravis,* and *G. newtoni* (1.620, 1.465, 1.342, 1.263, respectively; Fig. S15, Table S1B). The largest gastrolith size ratio, with respect to mean body mass, was *D. novaehollandiae*, followed by *D. robustus, E. c. gravis,* and *G. newtoni* (0.817, 0.756, 0.564, 0.495, respectively; Fig. S15, Table S1B).

The dromornithid *Genyornis newtoni* was the largest taxon, but when body size was accounted for, *G. newtoni* has the smallest ratios for gizzard mass and gastrolith size. *Dromaius novaehollandiae* has the largest gastrolith size ratio with respect to mean body mass, and the extinct G. *newtoni* and *E. c. gravis* have comparable gizzard mass and gastrolith size ratios.

Table S1. **A**, gastrolith size, gizzard mass, and body mass by taxon for Holocene NZ palaeognath moa: *Dinornis robustus*; *Euryapteryx curtus gravis*; Australian emu (*Dromaius novaehollandiae*) and dromornithid (*Genyornis newtoni*), for which complete gizzard data are associated. **B**, size-standardised gastrolith size and gizzard mass ratios, where $\log_{10}$ transformed species data were divided by $\log_{10}$ transformed specimen mean BM values (see **3.6.4**–**5**). **Abbreviations**, **BM**, body mass; **CB**, Lake Callabonna; **CM**, Canterbury Museum; **CU**, Callabonna Uncatalogued, field code, Flinders University fossil collection; **FB**, Frome Basin; **Fem L**, femur length; **FUR**, Flinders University Reference collection; **g**, grams; **GM**, gizzard mass; **GS**, gastrolith size; **HH**, Honeycomb Hill Cave; **kg**, kilograms; **MC**, Maximus Cave; **mm**, millimetres; **MS**, Moonsilver Cave; **NMNZ**, National Museum of New Zealand; **No**, number; **NZ**, New Zealand; **PV**, Pyramid Valley Swamp; **SAM**, South Australian Museum.

A. Taxon	Catalogue No	Site	Fem L (mm)	GS (mm)	GM (g)	BM [Range] (kg)
D. robustus	NMNZ S25765	HH ⸸	334	>40 ●	2450	154.92 [132.56–181.33]
D. robustus	CM 20118	PV ⸸	390	>40 ●	4380	255.42 [218.23–298.97]
D. robustus	NMNZ S23654	HH ⸸	303	>40 ●	2310	113.15 [96.67–132.44]
D. robustus	NMNZ S32678	MS ⸸	324	>40 ●	3080	140.45 [119.99–164.39]
D. robustus	NMNZ S28225	MC ⸸	265	>40 ●	2090	73.44 [62.74–85.96]
E. c. gravis	NMNZ 525656	HH ⸸	310	15 ♦	630	121.8 [104.06–142.10]
D. novaehollandiae	FUR 163	FB ☼	223	21.2 (n=5) ■	240	42.09[35.96–49.26]
G. newtoni	CU 2018-23	CB ☼	–	12.5 (n=5) ■	1270	219.8 *
G. newtoni	SAM P53833	CB ☼	355	15.4 (n=5) ■	540	188.59 [161.13–220.75]

B. Taxon	GS Ratio	GS Mean	GM Ratio	GM Mean	Log(GS)	Log(GS) Mean	Log(GM)	Log(GM) Mean	Log(BM)	Log(BM) Mean
D. robustus	0.731		1.547		1.602		3.389		2.190	
D. robustus	0.666		1.513		1.602		3.641		2.407	
D. robustus	0.780	0.756	1.638	1.620	1.602	1.602	3.364	3.441	2.054	2.133
D. robustus	0.746		1.624		1.602		3.489		2.148	
D. robustus	0.859		1.779		1.602		3.320		1.866	
E. c. gravis	0.564	0.564	1.342	1.342	1.176	1.176	2.799	2.799	2.086	2.086
D. novaehollandiae	0.817	0.817	1.465	1.465	1.326	1.326	2.380	2.380	1.624	1.624
G. newtoni	0.468	0.495	1.325	1.263	1.097	1.142	3.104	2.918	2.342	2.309
G. newtoni	0.522		1.201		1.188		2.732		2.276	

Alexander's [179] BM algorithms

BM: Fem L/270 = (BM/78)^0.31

Range: Fem L/270*1.05; Fem L/270/1.05 = (BM/78)^0.31

* mean mass estimation for *G. newtoni* 'unsexed data' (n = 22), based on tibiotarsus least-shaft circumference from Grellet-Tinner et al. [32] (table A2), see **S6.1**; ♦ [113]; ● [19]; ■ measured by WDH

⸸ South Island NZ site; ☼ South Australian site.